



Please cite the Published Version

Jokl, E, Mullan, AF, Simpson, K, Birchall, L, Pearmain, L, Martin, K, Pritchett, J , Raza, S, Shah, R, Hodson, NW, Williams, CJ, Camacho, E, Zeef, L, Donaldson, I, Athwal, VS, Hanley, NA and Piper Hanley, K  (2023) PAK1-dependent mechanotransduction enables myofibroblast nuclear adaptation and chromatin organization during fibrosis. *Cell Reports*, 42 (11). 113414 ISSN 2211-1247

DOI: <https://doi.org/10.1016/j.celrep.2023.113414>

Publisher: Elsevier BV

Version: Published Version

Downloaded from: <https://e-space.mmu.ac.uk/636574/>

Usage rights:  [Creative Commons: Attribution 4.0](https://creativecommons.org/licenses/by/4.0/)

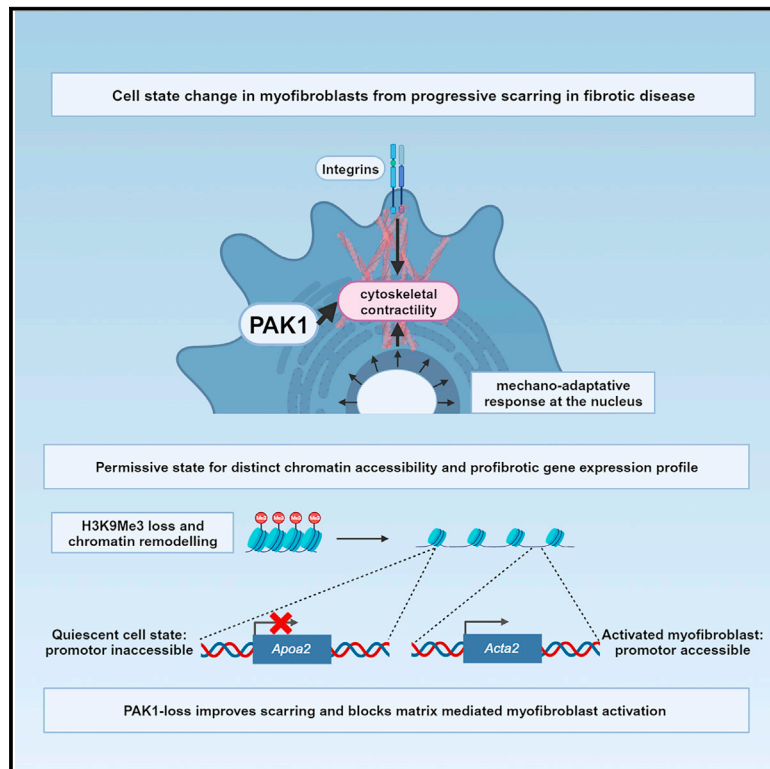
Additional Information: This is an open access article which first appeared in *Cell Reports*

Enquiries:

If you have questions about this document, contact openresearch@mmu.ac.uk. Please include the URL of the record in e-space. If you believe that your, or a third party's rights have been compromised through this document please see our Take Down policy (available from <https://www.mmu.ac.uk/library/using-the-library/policies-and-guidelines>)

PAK1-dependent mechanotransduction enables myofibroblast nuclear adaptation and chromatin organization during fibrosis

Graphical abstract



Authors

Elliot Jokl, Aoibheann F. Mullan, Kara Simpson, ..., Varinder S. Athwal, Neil A. Hanley, Karen Piper Hanley

Correspondence

karen.piperhanley@manchester.ac.uk

In brief

Jokl and Mullan et al. report mechanisms underpinning the profibrotic myofibroblast state during fibrosis involve nuclear softening and heterochromatin de-repression following H3K9me3 loss. They show this profibrotic switch can be reversed by uncoupling actomyosin signaling through *Pak1* deletion. This represents a targetable therapeutic pathway in fibrosis, with implications across organs.

Highlights

- Chromatin reorganization permits profibrotic gene expression in fibrosis
- Fibrosis induces nuclear softening and heterochromatin de-repression in myofibroblasts
- PAK1 enables mechanoadaptation of myofibroblasts in fibrosis
- PAK1 loss impairs myofibroblast contractility *in vitro* and reduces fibrosis *in vivo*



Article

PAK1-dependent mechanotransduction enables myofibroblast nuclear adaptation and chromatin organization during fibrosis

Elliot Jokl,^{1,2,9} Aoibheann F. Mullan,^{2,9} Kara Simpson,^{1,2} Lindsay Birchall,^{1,2} Laurence Pearmain,^{1,2} Katherine Martin,^{1,2} James Pritchett,³ Sayyid Raza,^{1,2} Rajesh Shah,⁴ Nigel W. Hodson,⁵ Craig J. Williams,⁶ Elizabeth Camacho,⁷ Leo Zeef,⁵ Ian Donaldson,⁵ Varinder S. Athwal,^{1,2,4} Neil A. Hanley,^{2,4,8} and Karen Piper Hanley^{1,2,10,*}

¹Wellcome Centre for Cell-Matrix Research, Faculty of Biology, Medicine & Health, Manchester Academic Health Science Centre, University of Manchester, Oxford Road, Manchester, UK

²Division of Diabetes, Endocrinology and Gastroenterology, Faculty of Biology, Medicine & Health, University of Manchester, Manchester Academic Health Science Centre, Oxford Road, Manchester, UK

³Department of Life Sciences, Manchester Metropolitan University, Manchester, UK

⁴Manchester University NHS Foundation Trust, Oxford Road, Manchester, UK

⁵Core Facilities, Faculty of Biology, Medicine & Health, University of Manchester, Manchester, UK

⁶Department of Materials, University of Manchester, Manchester, UK

⁷Division of Population Health, Health Services Research and Primary Care, School of Health Sciences, University of Manchester, Manchester, UK

⁸College of Medical & Dental Sciences, University of Birmingham, Birmingham, UK

⁹These authors contributed equally

¹⁰Lead contact

*Correspondence: karen.piperhanley@manchester.ac.uk

<https://doi.org/10.1016/j.celrep.2023.113414>

SUMMARY

Myofibroblasts are responsible for scarring during fibrosis. The scar propagates mechanical signals inducing a radical transformation in myofibroblast cell state and increasing profibrotic phenotype. Here, we show mechanical stress from progressive scarring induces nuclear softening and de-repression of heterochromatin. The parallel loss of H3K9Me3 enables a permissive state for distinct chromatin accessibility and profibrotic gene regulation. Integrating chromatin accessibility profiles with RNA expression provides insight into the transcription network underlying the switch in profibrotic myofibroblast states, emphasizing mechanoadaptive regulation of PAK1 as key drivers. Through genetic manipulation in liver and lung fibrosis, loss of PAK1-dependent signaling impairs the mechanoadaptive response *in vitro* and dramatically improves fibrosis *in vivo*. Moreover, we provide human validation for mechanisms underpinning PAK1-mediated mechanotransduction in liver and lung fibrosis. Collectively, these observations provide insight into the nuclear mechanics driving the profibrotic chromatin landscape in fibrosis, highlighting actomyosin-dependent mechanisms as potential therapeutic targets in fibrosis.

INTRODUCTION

Fibrosis in any organ is characterized by the deposition of pathological extracellular matrix (ECM) leading to progressive scarring and ultimately causing loss of organ function. In the liver, fibrosis is potentially reversible during early stages. However, liver fibrosis is almost always diagnosed too late with limited treatment options. There is a massive unmet clinical need to halt liver fibrosis.

Activated hepatic stellate cells (HSCs; liver-specific myofibroblasts) are responsible for scar production during progressive liver fibrosis.^{1–5} The physical scar increases tissue stiffness resulting in compromised tissue function that ultimately leads to liver failure.^{6–8} Despite increasing knowledge of important signaling pathways promoting HSC activation and expression of key profibrotic components,^{3,5,9–14} many are also active in the healthy liver, and

by themselves, or even in aggregate, they do not account for the complete phenotypic switch in cell state that distinguishes activated from quiescent HSCs. In recent years, we know that tissue stiffness can radically alter the cytoskeletal architecture of HSCs to influence cell behavior through cell surface integrin receptors.^{3,6,8,15} For example, loss of integrin- β 1 reduces the ability of HSCs to adhere firmly to profibrotic ECM, with reduced actin organization in the cytoskeleton.³ Downstream of integrin- β 1, the serine/threonine-protein kinase P21-activated kinase group (PAK; associated with actomyosin signaling) and the transcriptional co-activator Yes-associated protein-1 (YAP1) are mechanosensing mechanisms responsible for myofibroblast activation and liver fibrosis.^{3,9} Although informative, it is becoming increasingly evident that mechanical signals reach beyond the cytoskeleton toward the nucleus to induce a rapid profibrotic physiological response.^{16,17}



The nucleus is enclosed by the nuclear envelope (NE) composed of an outer and inner nuclear membrane.^{17,18} The nuclear lamina (NL) is a lining on the inner nuclear membrane that contains lamin proteins, which provide elasticity to the NE allowing the nucleus to adapt to mechanical stimuli.^{16–18} The NE is connected to the cytoskeleton by the linker of nucleoskeleton and cytoskeletal (LINC) complex of proteins, which also connects to the NL.¹⁹ Thus, the cytoskeleton, intimately linked to intracellular tension, is connected to the NL. Moreover, some genomic regions, called lamina-associated domains (LADs), are anchored to the NL.²⁰ In mammalian cells, LADs can cover >30% of the genome and are generally associated with genome repression and heterochromatin marks such as lamina-associated histone H3 tri-methyl lysine 9 (H3K9Me3).²¹ Thus, it becomes easy to conceive how cell tension, as increases during HSC activation, might alter spatial organization of the genome and transcription.^{18,22} This represents an under-researched and emerging area for targeted antifibrotic therapy. However, to facilitate this research requires investigation in clinically relevant cellular models to avoid confounding factors associated with epigenetic mechanical memory from prolonged primary cell culture or use of cell lines.

Here, in freshly isolated liver HSCs, we begin from the perspective that liver myofibroblasts undergo a radical transformation in cell shape and state linked to an increasingly profibrotic phenotype. Our data identify nuclear softening and de-repression of heterochromatin following H3K9Me3 loss as a permissive state for distinct chromatin accessibility and profibrotic gene regulation. We discovered this profibrotic phenotypic switch could be reversed by uncoupling actomyosin signaling through *Pak1* deletion. *In vivo*, *Pak1* loss during liver fibrosis improved scarring and blocked matrix-mediated myofibroblast activation. Through integrative analysis of RNA and assay for transposase-accessible chromatin (ATAC) sequencing data, we provide detailed understanding of the transcriptional networks and open chromatin landscape underlying the switch in profibrotic myofibroblast cell states, emphasizing mechanoadaptive pathways linked to PAK1 as key drivers. As a core PAK1-dependent mechanism, we provide further *in vitro* and *in vivo* evidence in models of lung fibrosis. Pathways capable of blocking or reversing this response represent highly desirable antifibrotic agents with implications across organ fibrosis.

RESULTS

PAK1-dependent signaling promotes myofibroblast activation in human and mouse models of fibrosis

During liver fibrosis, increasing tissue stiffness induced by the pathological scar activates HSCs.^{3,6,8} The *in vitro* model for activating HSCs on tissue culture plastic exemplifies this.^{3,11,14} We have previously described PAK1 as the predominant group I PAK family member detected during HSC activation *in vitro*.³ In keeping with our previous work, this elevated expression in activated HSCs also corresponded to increased levels of phosphorylated PAK1 indicative of an active protein state (Figures S1A and S1B). To understand the pathophysiological role of PAK1 in fibrosis, we initially modeled liver fibrosis in mice using carbon tetrachloride (CCl₄) injections to induce parenchymal injury and

bile duct ligation (BDL) for biliary injury. In both models, *Pak1* transcript was detected in elongated cells, characteristic of activated HSCs, localized to and within the fibrotic scar (Figures 1A–1C). *Pak1* transcripts were also evident in hepatocytes parallel to the scar (particularly during BDL-induced fibrosis). These data are similar to our previous work indicating hepatocytes aligning the scar undergo a regenerative response indicative of the ductal plate during liver development.⁹ Consistent with our observations in HSCs, liver lysate from mice with fibrosis due to CCl₄ or BDL corresponded to increased phosphorylated PAK1 protein levels (Figures S1C and S1D). In sections of human liver cirrhosis, PAK1 protein was localized to PDGFR β -positive fibrotic areas indicating its relevance to human liver disease (Figure S1E). Given these similarities across species, we next determined the importance of PAK1 in progression of liver fibrosis using our mouse model system to investigate the consequence of *Pak1* loss during fibrosis. Liver weight and toxicity (assessed in serum by ALT and bilirubin levels) were unaltered following *Pak1* loss (Figures S1F–S1J). In livers from CCl₄-induced fibrosis, fibrotic collagen deposition was significantly reduced in the hepatic parenchyma by picro sirius red (PSR) staining following *Pak1* loss (Figures 1D and 1E). Moreover, loss of *Pak1* also decreased the amount of alpha smooth muscle actin (α -SMA) staining in the liver implying reduced myofibroblast activation (Figures 1D and 1F). Similarly, in BDL-induced liver fibrosis, the marked peribiliary collagen deposition was greatly improved alongside reduced α -SMA staining and ductal hyperplasia (a feature of biliary injury shown by cytokeratin-19 [CK19] analysis) in *Pak1*-null animals (Figures 2A–2D). To determine the importance of PAK1 in broad mechanisms associated with myofibroblast activation in fibrosis, PAK1 was absent from healthy human lung but was robustly detected in regions of human lung fibrosis due to idiopathic pulmonary fibrosis (Figure S2A). As a second *in vivo* validation model, we carried out bleomycin-induced lung fibrosis in *Pak1*-null animals. Similar to liver, compared to control mice, loss of *Pak1* significantly improved the extent of collagen deposition and fibrosis (Figures S2B and S2C). These data support PAK1 as a core regulator of myofibroblast activation during fibrosis and suggest mechanistic insight may highlight PAK1-dependent pathways as targets to improve fibrosis therapeutically.

Mechanical stress and profibrotic response are transmitted via PAK1 in liver myofibroblasts

To probe the mechanisms underlying PAK1 function in myofibroblasts, we extracted HSCs from wild-type (WT) and *Pak1*-null livers and cultured on plastic for 7–10 days to model myofibroblast activation with the appearance of α -SMA, sex determining region Y-box 9 (SOX9), and the major fibrotic ECM protein, collagen type 1 (COL1).^{11,13,14} Consistent with the *in vivo* data, following culture on plastic, *Pak1*-null activated HSCs had a reduction in the classical fibrotic markers α -SMA, COL1, and SOX9 (Figure S2D). Moreover, in line with our previous work,³ *Pak1*-null HSCs displayed reduced amounts of integrin- β 1, integrin alpha 11 (ITGA11), and focal adhesion kinase (FAK) proteins, suggesting impaired ECM sensing (Figure S2D). More broadly, transcriptomic analysis showed *Pak1* loss did not convert cells back to a quiescent phenotype but a largely intermediate state consistent with

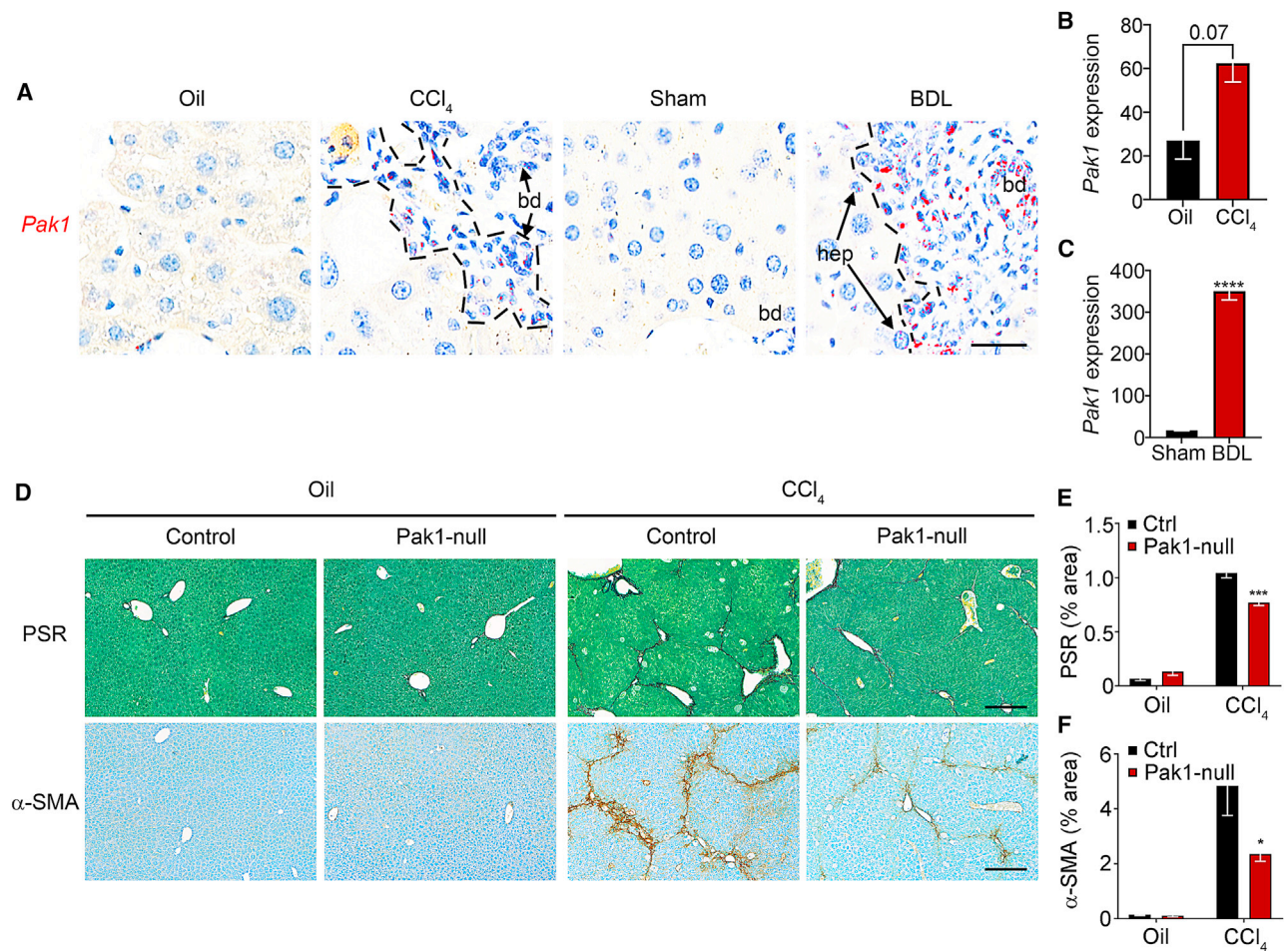


Figure 1. *Pak1* is localized to fibrotic scars, and its loss *in vivo* improves CCl₄-induced liver fibrosis

(A) Representative images of *Pak1* transcript (red) localized to cells within the fibrotic scar (hatched line) in both CCl₄- and BDL-induced liver fibrosis *in vivo*. bd, bile duct indicated; hep, hepatocytes. Bar, 25 μ m.

(B and C) Quantification of average *Pak1* transcripts per field of view (FOV) in CCl₄ and BDL models of liver fibrosis compared to control (n = 20 FOV per animal, and n = 3 animals per group).

(D) PSR staining (collagen deposition in red) counterstained with fast green (top row) and α -SMA (brown) counterstained with toluidine blue (bottom) in olive oil (Oil) or chronic CCl₄-induced fibrosis in control and *Pak1*-null mice (n = 5 animals per group). Bar, 500 μ m.

(E and F) Quantification of surface area covered by PSR staining in (E) and α -SMA in (F) from representative image in (D). Means \pm SEM. *p < 0.05, ***p < 0.005, ****p < 0.001. Data analyzed using one-way ANOVA with Tukey's post hoc test for (D) and (E). Two-tailed unpaired t test was used to analyze (B) and (C).

our previous work on HSCs lacking integrin- β 1 (upstream of PAK1; Figure S2E; Table S1).³ To identify gene regulatory pathways responsible for the reduced profibrotic phenotype in *Pak1*-null myofibroblasts, we carried out hierarchical cluster analysis (Figure S2E). From eight clusters, we focused our attention to cluster 5 with consistent reduction in differentially expressed genes following *Pak1* loss in both quiescent and activated HSC populations (Figure S3A). Significantly, the top twenty Gene Ontology terms were involved in contractility, ECM, and cytoskeletal signaling (Figure S3B).

In keeping with these data, stress fibers (marked by F-actin) were impaired, and the myofibroblast-like appearance was lost in *Pak1*-null HSCs, which had a rounded (more quiescent-like) phenotype (Figure 3A). Similarly, *Pak1*-null cells displayed significantly reduced F-actin intensity compared to control cells using

live cell imaging of fluorescently labeled endogenous F-actin (Figures 3B and 3C), indicative of disrupted actin polymerization. *Pak1* loss in activated myofibroblasts also disabled collagen gel contraction (Figures 3D and 3E). To assess cell migration, we used 24-h single-cell tracking of *Pak1*-deficient compared to control myofibroblasts. Although no marked difference in cell migration was detected in terms of total track length, the directionality of migration in *Pak1*-null HSCs was significantly perturbed. Positional analysis of individual cells over time showed control HSCs moved persistently over long periods, whereas *Pak1*-null HSCs failed to undergo directional migration and frequently changed direction to display a focal migratory pattern (i.e., limited movement from the point of origin) (Figures 3F–3I, S4A, and S4B). To investigate this further, we explored whether the disrupted actin cytoskeleton impaired myofibroblast polarization important for nuclear

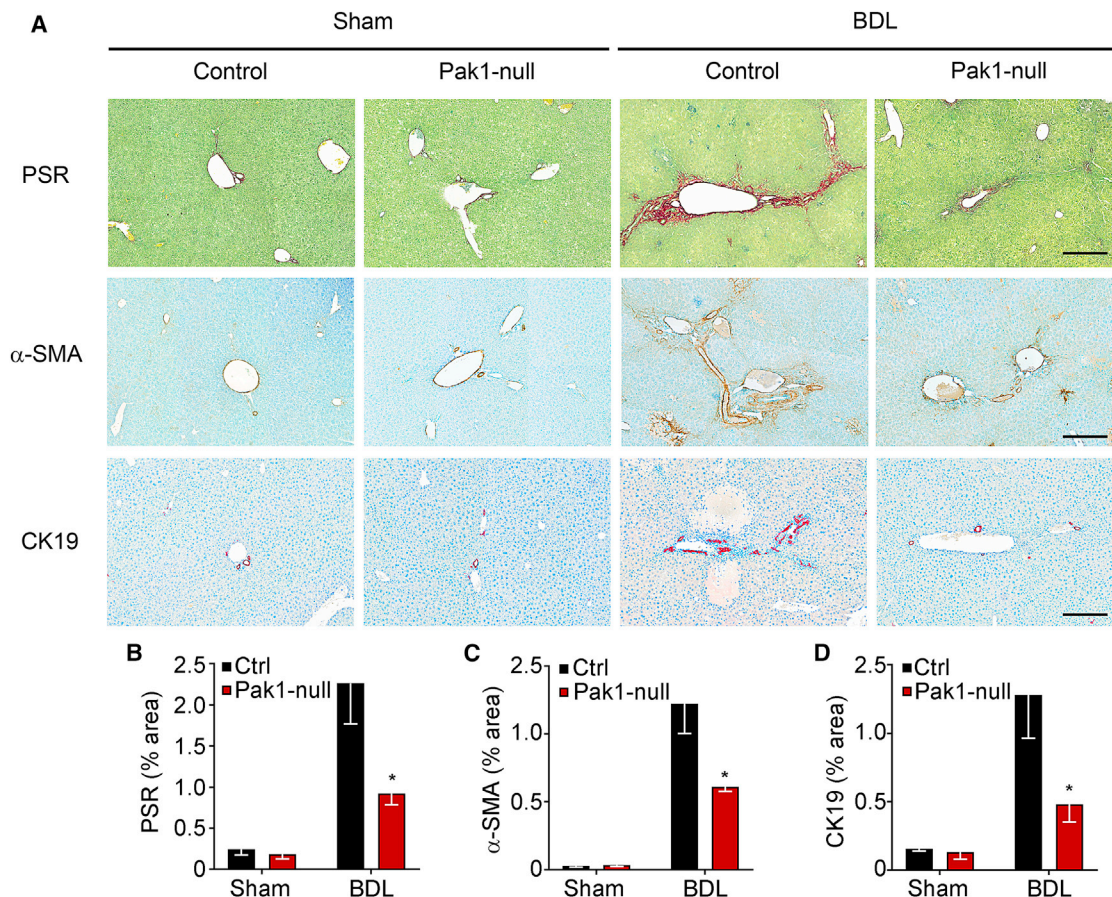


Figure 2. *Pak1* loss improves biliary fibrosis *in vivo*

(A) PSR staining (collagen deposition in red) counterstained with fast green (top row), α -SMA (brown; middle row), and CK19 (brown; bottom row) counterstained with toluidine blue in sham operation (sham) or BDL-induced fibrosis in control and *Pak1*-null mice ($n = 5$ animals per group). Bar, 500 μ m.

(B and D) Quantification of surface area covered by PSR staining in (B), α -SMA in (C), and CK19 in (D) from representative image in (A). Means \pm SEM. * $p < 0.05$. Data analyzed using one-way ANOVA with Tukey's post hoc test.

orientation in cell migration. Control and *Pak1*-null activated HSCs were plated onto fibronectin-coated, bow-shaped micropatterns to recapitulate patterning required in classical front-rear polarization. Following culture and staining for the actin cytoskeleton, although descriptive, there appeared to be a failure in cytoskeletal organization of cells lacking *Pak1* potentially leading to an altered nuclear orientation (Figures 3J and 3K).

HSCs lacking *Pak1* are unresponsive to their physical environment

Mechanical forces transmitted through the cell directly influence nuclear shape and function responsible for altered gene expression. To explore the mechanical behavior of activated HSCs, we placed cells in a restricted physical environment and used YAP1 localization as a mechanical readout. Following culture activation, control or *Pak1*-null HSCs were placed on fibronectin-coated circular micropatterns. As expected, YAP1 localization in control HSCs was predominantly nuclear on large micropatterns (Figures 4A and S4C). In contrast, *Pak1*-null HSCs displayed much reduced and limited YAP1 nuclear localization par-

alleled by a disrupted actin cytoskeleton marked by α SMA, indicative of impaired cell spreading and mechanical signaling (Figures 4A and S4C).

To provide insight from a physiologically relevant fibrotic environment, activated control or *Pak1*-null HSCs were cultured on hydrogels with differing stiffness to model physiologically normal liver elasticity (4 kPa) or the fibrotic environment (12 kPa). Little difference in YAP1 localization was observed between control and *Pak1*-null HSCs at 4 kPa; however, interestingly, the profibrotic marker α SMA appeared more pronounced in control cells, highlighting early cytoskeletal alterations following *Pak1* loss (Figure 4B). HSCs cultured on 12 kPa maintained the altered α SMA appearance, whereas YAP1 nuclear localization was greatly diminished in *Pak1*-null cells (Figures 4B and 4C). In support, *Pak1*-null cells displayed reduced RNA levels of *Yap1* and diminished phosphorylation of the direct downstream target MYL9 (Figures 4D and 4E), important in promoting actomyosin interactions and force generation. Mechanistically, PAK1 has been linked to Merlin/NF2 phosphorylation and subsequently alleviating its negative regulation of YAP1.²³ In line with this,

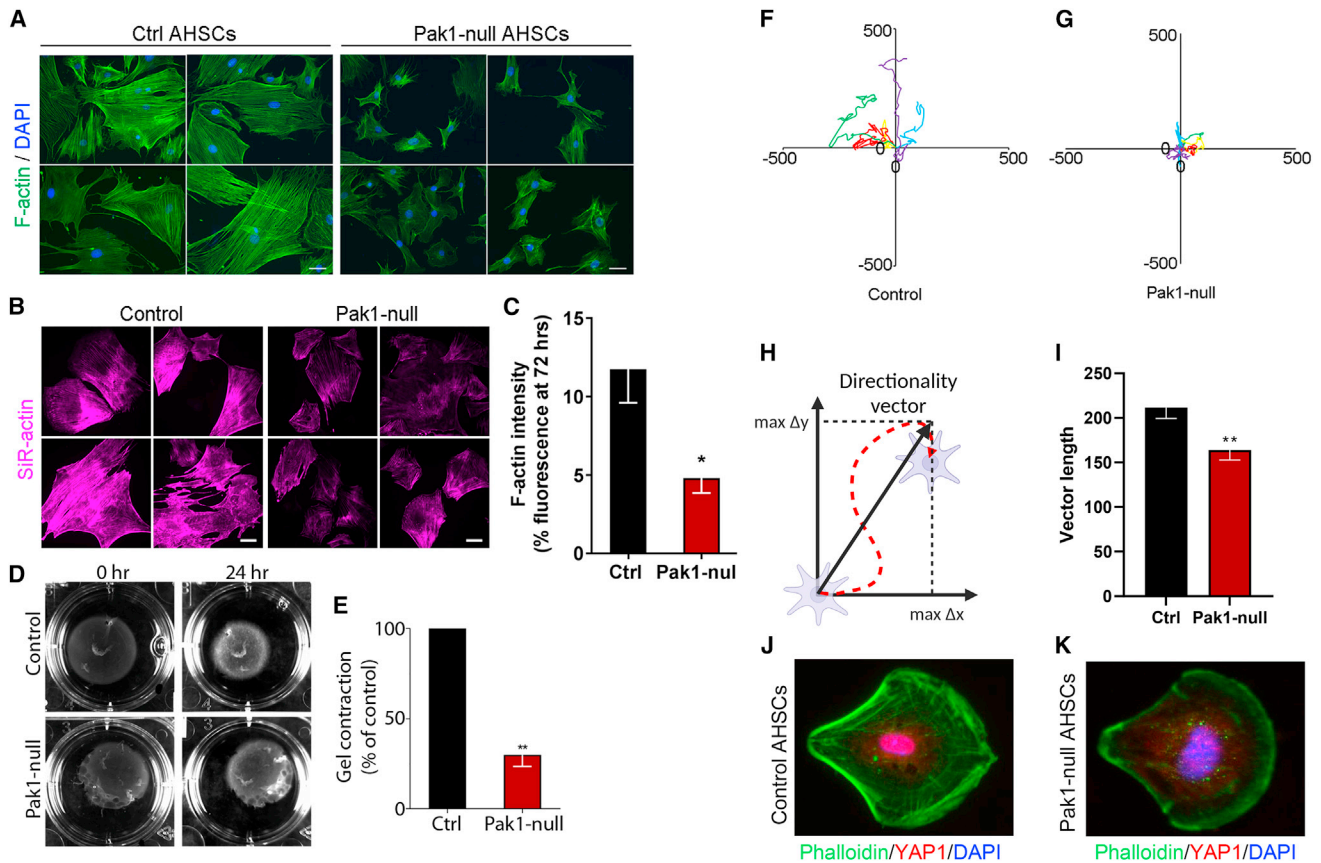


Figure 3. Functional characterization of liver myfibroblasts lacking *Pak1*

(A) Immunofluorescence staining for F-actin (green) and nuclei (DAPI; blue) in control and *Pak1*-null activated HSCs (AHSCs). (B and C) Live F-actin labeling in live control and *Pak1*-null AHSCs imaged at 72 h. Example images are shown in (B) with fluorescence intensity quantification in (C) from three biological replicates with 15 cells per experiment analyzed. (D and E) Contractile properties of control and *Pak1*-null AHSCs assessed by gel contraction assay. Representative image is shown in (D), and quantification from three biological experiments is shown in (E). (F–I) Live cell migration over 24 h from control and *Pak1*-null AHSCs. (F and G) Example track length shown (data from three biological replicates and 15 cell tracks). (H and I) Schematic demonstrating cell directionality assessed by the hypotenuse length of the triangle defined by the magnitude of movement in the x and y axes (H) and graphical representation (I). (J and K) Immunofluorescence for F-actin (green), YAP-1 (red), and nuclei (DAPI; blue) in control and *Pak1*-null AHSCs cultured on cross-bow micropatterns for 24 h. Representative images of three independent experiments. Means \pm SEM; n = 3 biological replicates. *p < 0.05, **p < 0.01 by two-tailed t test. Bar, 5 μ m. See also Figure S4.

activated HSCs lacking *Pak1* have reduced NF2 phosphorylation (Figure 4F).

Myfibroblast activation induces a radically altered cell state associated with nuclear adaptation

Collectively our data indicated myfibroblasts lacking PAK1 were less fibrotic and unresponsive to their physical environment through perturbed cytoskeletal and mechanosignaling. To explore how the physical environment alters myfibroblast cell state, we modeled the increasing profibrotic response in culture-activated HSCs at 1, 3, 5, 7, and 10 days. In addition to the characteristic cytoskeletal shape change (Figure S5A),^{3,11,14} we uncovered nuclear size was increased as HSCs activate (Figures 5A, 5B, S5A, and S5B). In parallel, DAPI intensity was noticeably reduced, suggesting altered chromatin organization (Figures 5C, S5A, and S5B). Following exponential regression analysis, there was a sta-

tistically significant relationship, suggesting nuclear area explains 96% of the variance in DAPI intensity (Figure 5C; $R^2 = 0.96$; p < 0.001). These data were similarly recapitulated in culture-activated lung fibroblasts, suggestive of similar state changes at the cellular level in lung, potentially indicating broad function in organ fibrosis (Figures S5C–S5F). To explore the impact of this mechanoadaptive response, we used atomic force microscopy (AFM) to assess the physical properties of the nucleus and discovered activated myfibroblasts have reduced nuclear stiffness in response to a stiff environment (Figure 5D).

To understand this adaptive response further, we used our physiologically relevant *Pak1*-null HSC model to uncouple actomyosin and, in part, alleviate the mechanical stress response. We first focused on the composition of the NE. Lamina proteins, including lamin A/C (LMNA/C) and lamin B1 (LMNB1), line the inside of the NE, where disruption of their function and composition

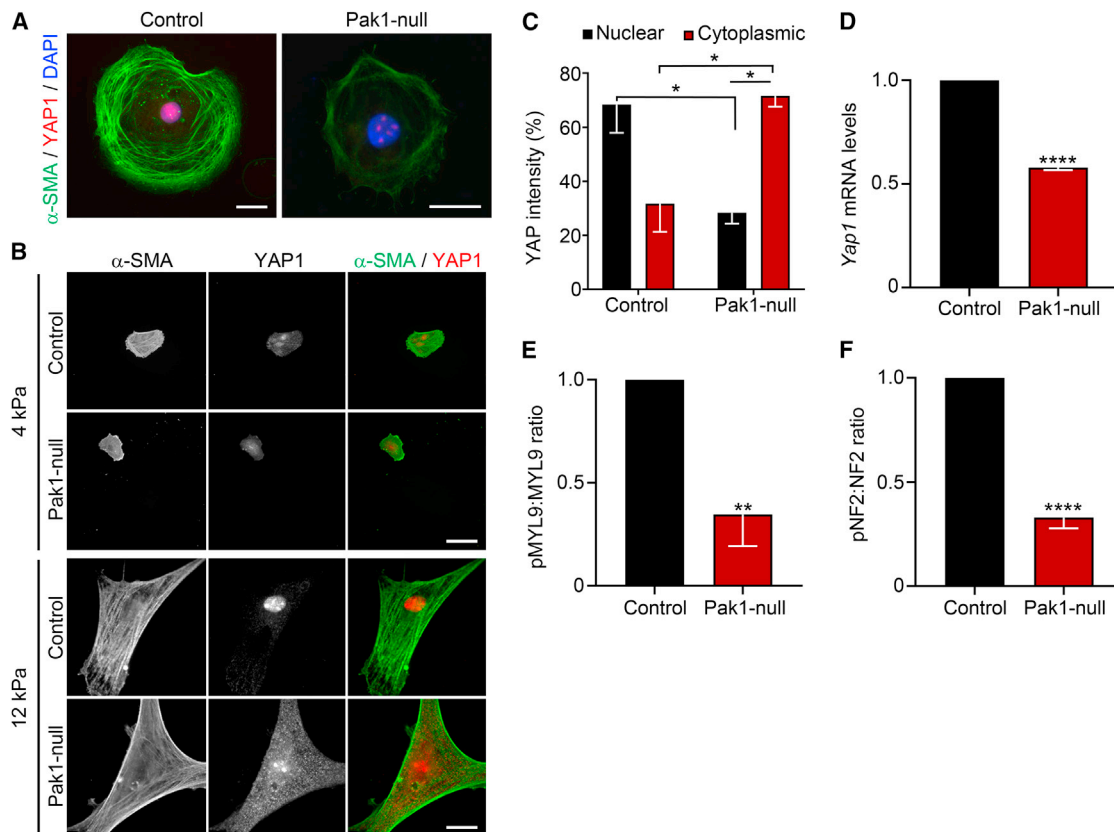


Figure 4. Mechanical response is impaired in *Pak1*-null liver myofibroblasts

(A) Immunofluorescence staining for α -SMA (green), YAP1 (red), and nuclei (DAPI; blue) in control and *Pak1*-null AHSCs cultured on circular micropatterns for 24 h. Representative images of three independent experiments.

(B and C) Immunofluorescence showing individual and merged images for α -SMA (green) and YAP1 (red) in control and *Pak1*-null AHSCs cultured on hydrogels at 4 and 12 kPa. Representative image in (B) and quantification in (C) showing the average intensity of nuclear and cytoplasmic YAP1 fluorescence of three biological replicate experiments from 15 cells analyzed per experiment.

(D) Quantification and relative levels of Yap1 mRNA in control and *Pak1*-null AHSCs.

(E and F) Protein quantification and phosphorylation ratios shown for pMYL9 to total MYL9 (pMYL9:MYL9) in (E) and pNF2 to total NF2 (pNF2:NF2) in (F). Means \pm SEM; n = 3 biological replicates. *p < 0.05, **p < 0.01, ****p < 0.001. Data analyzed using one-way ANOVA with Tukey's post hoc test (C) and two-tailed t test (D–F). Bar, 10 μ m. See also Figures S8 and S4.

can lead to altered nuclear morphology and gene expression.²⁴ Increased LMNA/C has previously been associated with cells cultured on stiff matrices.²⁵ Whereas, from our genomic datasets, *LmnA* and *LmnB1* are both highly expressed in activated HSCs (Figures S5G–S5J; Table S1). Although little difference was detected at the transcript level (Table S1), at the protein level, we observed equivalent LMNA/C (Figure 5E), whereas LMNB1 was almost double in *Pak1*-null HSCs (Figure 5F). Using AFM, we tested how these changes related to nuclear stiffness. Compared to control HSCs, loss of *Pak1* induced nuclear stiffening (Figures 5G and 5H). In parallel, culturing activated *Pak1*-null HSCs on hydrogels decreased nuclear area at physiologically relevant liver stiffness, consistent with an impaired mechano-response (Figures 5I and 5J). These data were reminiscent of a quiescent phenotype observed in our profile of HSC activation over time (Figure 5A), further emphasizing the critical role of PAK1-dependent signaling in the profibrotic response of myofibroblasts. Moreover, to support these mechanisms of contrac-

tility on nuclear response, we observed a similar reduction in nuclear size through blebbistatin treatment of the HSC human cell line, LX2 cells. Whereas, LPA treatment to increase cellular tension resulted in increased nuclear area in both WT HSCs and *Pak1*-null HSCs (Figures S5K–S5O). Combined, these observations suggested our *Pak1*-null phenotype was consistent with reduced contractility/cellular tension.

H3K9Me3 loss promotes nuclear remodeling and chromatin organization in myofibroblasts during fibrosis

We next wanted to understand how cell state changes at the nucleus affected chromatin organization and the phenotypic profibrotic gene expression. Mechanistically, we observed loss of the heterochromatin marker H3K9Me3 as HSCs activate (Figure 6A). Similarly, protein expression of H3K9Me3-associated methyltransferase, suppressor of variegation 3–9 homolog 1 (SUV39H1), was also decreased (Figure 6B). In mouse models of liver fibrosis, H3K9Me3 maintained robust expression in hepatocytes and bile

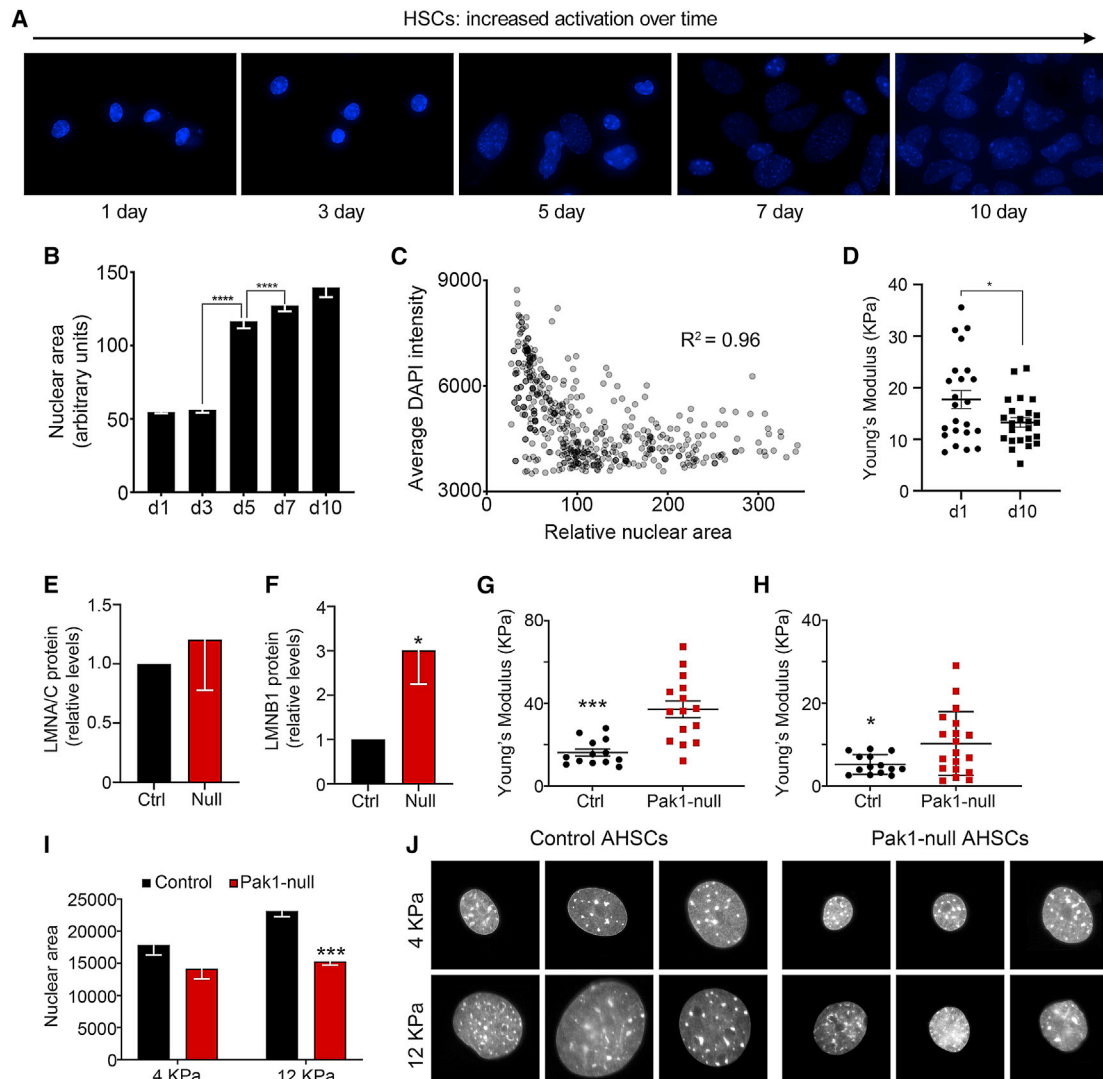


Figure 5. Altered cell state during liver myfibroblast activation

(A and B) Representative DAPI (blue) images of HSC nuclei in (A) and quantification of nuclear area during HSC activation on plastic over time in days from quiescent (d1) to activated (d10) in (B).
 (C) Graphical representation of all cells from (B) and inverse correlation of average DAPI intensity with nuclear size ($R^2 = 0.96$; $p < 0.001$).
 (D) Nuclear stiffness measurements displayed as kPa using AFM in quiescent (d1) and activated (d10) HSCs.
 (E and F) Protein quantification of LMNA/C in (E) and LMNB1 in (F) in control and *Pak1*-null AHSCs.
 (G and H) Nuclear stiffness measurements displayed as kPa using AFM in fixed in (G) and live in (H) control and *Pak1*-null AHSCs (d5).
 (I and J) Quantification in (I) and representative DAPI images in (J) of nuclear area in control and *Pak1*-null AHSCs cultured on hydrogels at 4 and 12 kPa. Means \pm SEM; $n = 3$ biological replicates. * $p < 0.05$, *** $p < 0.005$, and **** $p < 0.001$. Data analyzed using one-way ANOVA with Tukey's post hoc test (B) and two-tailed t test (D-I). See also [Figures S5](#) and [S8](#) and [Table S1](#).

ducts, whereas expression in myfibroblasts displayed lower H3K9Me3 intensity within the vimentin (VIM)-positive nuclei associated with the scar compared to the surrounding tissue ([Figures 6C](#), [6D](#), and [S6A](#)). Significantly, this altered nuclear cell state parallels a profibrotic switch in gene expression. From single-cell transcriptomics studies,^{26,27} core signatures associated with quiescent and activated HSCs were faithfully recapitulated in our genomic datasets ([Figures S5G–S5J](#); [Table S1](#)). Whereas, signatures associated with collagen and ECM modifications were highly induced alongside mechanotransduction pathways ([Figures S5I](#) and [S5J](#)),

emphasizing the environment and intracellular response as critical mediators of the observed physiological response at the nucleus. To explore this further and to understand how mechanical stress promotes H3K9Me3 heterochromatin function and nuclear properties of myfibroblasts, we analyzed the levels of H3K9Me3 and the methyltransferases SUV39H1 following *Pak1* loss. Following HSC activation, we uncovered increased levels of H3K9Me3 and SUV39H1 in *Pak1*-null compared to control HSCs indicative of a repressed chromatin state, reminiscent of quiescent HSCs ([Figures 6E–6G](#)). Similarly, *in vivo* activated HSCs isolated from

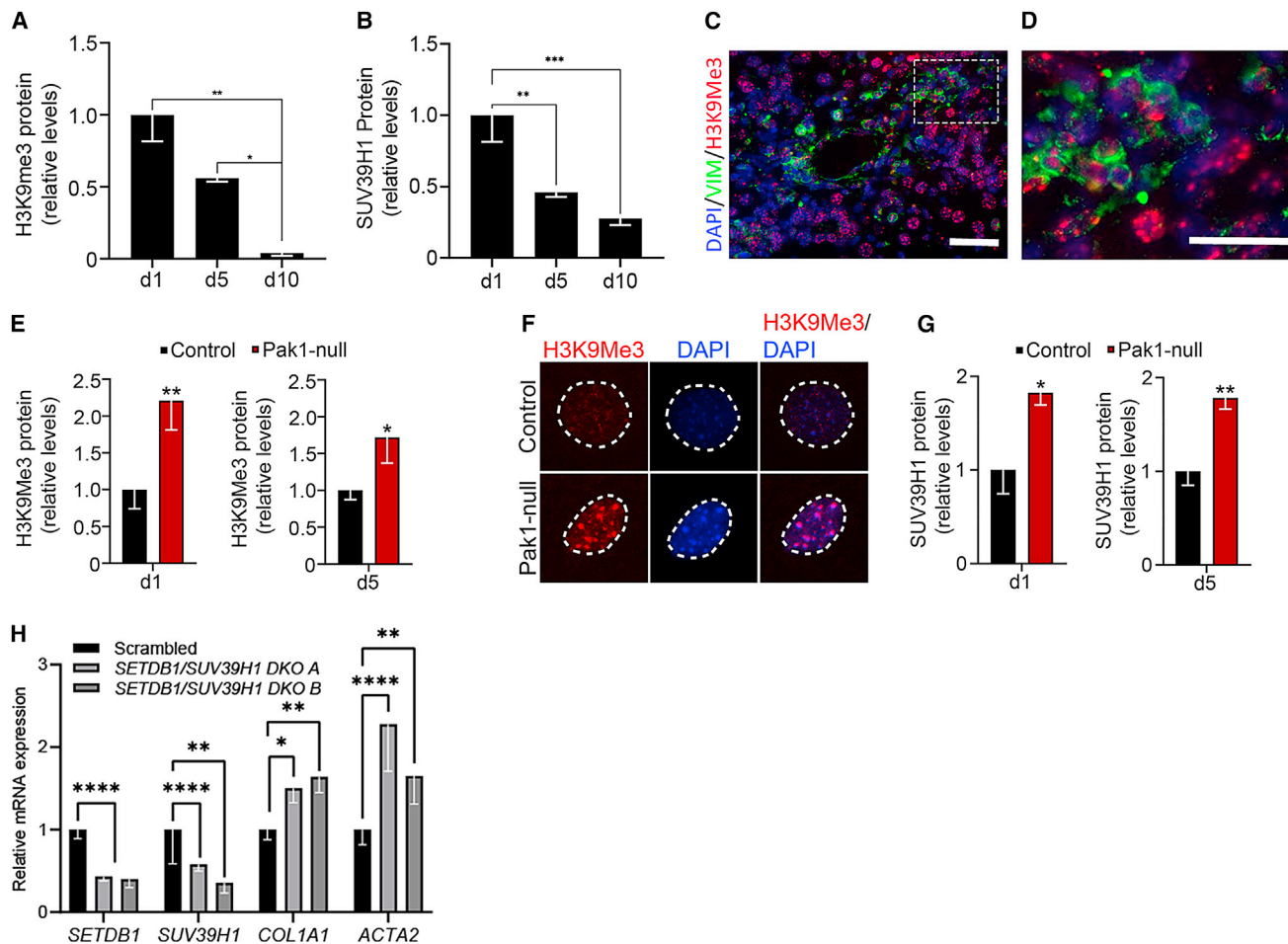


Figure 6. H3K9Me3 loss is associated with profibrotic myofibroblasts

(A and B) Quantification of H3K9me3 and SUV39H1 proteins during HSC activation.

(C and D) Immunofluorescence showing lower level H3K9Me3 (red) associated with VIM-positive (green) myofibroblasts in sections of murine liver fibrosis; DAPI (blue). Boxed area in (C) is magnified in (D).

(E and F) Protein quantification of H3K9Me3 in (E) and representative immunofluorescence staining for H3K9Me3 (red) and nuclei (DAPI; blue) in (F) in control and *Pak1*-null AHSCs. Hatched white line in (F) indicates external surface of nucleus.

(G) Quantification of SUV39H1 protein in control and *Pak1*-null AHSCs.

(H) Increased RNA levels of profibrotic markers *COL1A1* and *ACTA2* following abrogation of *SETDB1* and *SUV39H1* methyltransferases. Two independent siRNA pools are shown (A and B) relative to their respective scrambled control levels. Means \pm SEM; $n = 3$ biological replicates. * $p < 0.05$, ** $p < 0.01$, **** $p < 0.001$. Data were analyzed using one-way ANOVA with Tukey's post hoc test (A, B, and H) and two-tailed t test (E and G). Bar, 20 μ m. See also Figures S6, S9, and S10.

Pak1-null mice following acute CCl_4 -induced liver injury showed a reduced fibrotic phenotype and increased levels of SUV39H1 compared to control mice (Figures S6B and S6C).³ To further validate the link between H3K9Me3 methyltransferase activity and HSC activation, simultaneous siRNA knockdown of *SUV39H1* and *SETDB1* in the LX2 HSC human cell line resulted in elevated *COL1A1* and *ACTA2* transcript, consistent with a more activated state (Figure 6H).

Gene de-repression following H3K9Me3 loss correlates with a distinct profibrotic gene regulatory network

To investigate the chromatin accessibility and distinct gene regulatory networks associated with profibrotic myofibroblasts, we analyzed the genome-wide distribution of H3K9Me3 in the two

distinct states of liver HSCs, quiescent and activated, using CUT&TAG. Following sequencing, we characterized the dynamic distribution of H3K9Me3 peaks from two distinct antibodies. Consistent with our *in vitro* and *in vivo* data, using MACS2 peak calling, genome-wide enrichment of H3K9Me3 was detected in quiescent HSCs compared to activated HSCs (Figures S6D and S6E). As further validation, we used sparse enrichment analysis (SEACR), a peak caller method designed for processing CUT&TAG data. Similar to MACS2, SEACR identified an average of 15,666 total peaks in quiescent compared to only 3,113 in activated HSCs across the two independent antibodies. We assumed this would correlate with repression of activation-associated genes; however, the H3K9Me3 enrichment observed in quiescent HSCs appeared indiscriminately distributed between promoters of both

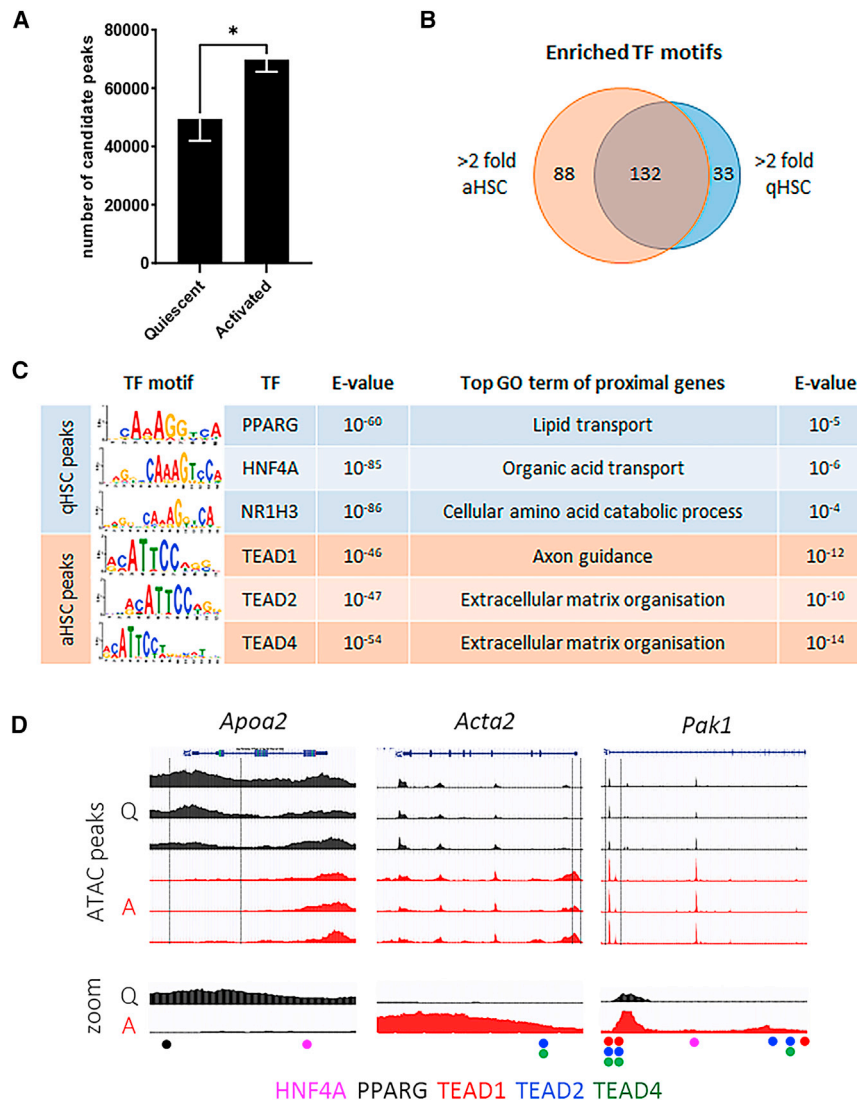


Figure 7. Chromatin organization correlates with profibrotic gene regulatory networks

(A) Significantly higher number of candidate ATAC peaks in activated cells.

(B) Venn diagram of TF motifs identified by simple enrichment analysis of ATAC peaks with >2-fold higher concentration in activated HSCs (aHSCs) or quiescent HSCs (qHSCs). 88 motifs are unique to aHSCs, 33 are unique to qHSCs, and 132 are common to both.

(C) Selected TF motifs along with e-value for enrichment and the top Gene Ontology biological functions returned based on the list of proximal genes to motif-containing peaks.

(D) ATAC tracks showing chromatin accessibility in quiescent (Q) and activated (A) HSCs. *Apoa2* shows increased accessibility in the quiescent state; conversely *Acta2* and *Pak1* show increased accessibility in the activated state. Indicated motifs from selected TFs from (C) in zoomed image (bottom tracks). Means \pm SEM; $n = 3$ biological replicates. * $p < 0.05$, by two-tailed t test. See also Table S2.

quences of all ATAC peaks that showed greater than 2- or less than -2-fold peak concentration in the activated HSCs compared to quiescent. This was followed by Gene Ontology analysis of genes proximal to ATAC peaks. As expected, many motifs were common to both quiescent and activated HSC states; however, 88 were unique to the activated state, including TEAD1, TEAD2, and TEAD4, and 33 were unique to the quiescent state, including PPARG, NR1H3, and HNF4A (Figures 7B and 7C; Table S2). Indeed, HNF4A and PPARG sites are evident around the promoter of *Apoa2*, which is more open in the quiescent state (Figure 7D). Similarly, TEAD2 and TEAD4 sites are evident around the promoter of *Acta2*, which is more open in activation (Figure 7D). Significantly and in keeping with our data suggesting PAK1 is critical mediator of mechanoadaptive pathways in HSC states, several TEAD sites were present around the promoter of *Pak1* (Figure 7D).

Understanding the transcription factor networks driving myofibroblast cell state

Further integration of our RNA-seq and ATAC-seq data provided a more detailed understanding of how gene expression is regulated in each HSC state (Figure S7A). Focusing on ATAC peaks at gene promoters, we used sequential filtering to generate gene lists based on significant alteration of promoter peak concentration and RNA expression in each state (Figure S7B; Table S3). Gene Ontology enrichment identified that genes with a more open chromatin profile and upregulated in activated HSCs (OAU) were enriched for ECM organization, in line with their profibrotic role. Whereas, genes more open and upregulated in

quiescence- and activation-associated genes (Figure S6F). These data suggested that although H3K9Me3 marks alone may not provide bespoke gene silencing in HSCs, de-repression of heterochromatin following H3K9Me3 loss provides a permissive state for distinct chromatin accessibility and profibrotic gene regulation in activated HSCs. To further understand how chromatin reorganization correlates with gene regulatory networks, we carried out parallel ATAC-seq and RNA-seq on quiescent and activated HSCs. Candidate regions of open chromatin “peaks” were identified using MACS2. Using differential binding analysis, chromatin accessibility profiles showed cell-state specificity with gene expression. Significantly, activated HSCs displayed a greater number of ATAC-seq candidate peaks, implying chromatin in activated HSCs was more globally accessible (Figure 7A), consistent with H3K9Me3 loss.

To determine the transcriptional networks underlying the quiescent and activated HSC states, we initially undertook simple enrichment analysis of transcription factor (TF) motifs in the se-

quiescent HSCs (OQUQ) displayed enrichment for lipid metabolism, recapitulating classical quiescent phenotype (Figure S7C). Interestingly, the transcription factors *Gfi1*, *Sall1*, and *Zeb1* associated with establishing H3K9me3-based heterochromatin domains were increased in the quiescent state compared to activated HSCs (Table S2). Moreover, *Sall1* appeared more accessible with increased regions of open chromatin in qHSCs (OQUQ; Table S3).

By combining motif enrichment at promoter peaks with respective RNA expression, we generated a regulatory TF network associated with the quiescent and activated HSC state. This highlighted HFF4A, IRF7, and STAT1/2 among others (Figure S7D) as enriched in the promoters of OQUQ genes and expressed more highly in the quiescent state. Similarly, ATF3, FOSL2, and CREB3/5 were among those enriched in the promoters of OUA genes and expressed more in the activated state (Figure S7D). Interestingly, overlaying our *Pak1*-null quiescent HSC genomic dataset with these defined TF networks showed significantly higher expression of several quiescent-associated TFs, including STAT1/2 and FLI1 (Figures S7E–S7G; Tables S4 and S5). These results provide further evidence that *Pak1*-null HSCs have a more quiescent transcriptional state, which may underlie their reduced mechanosensitivity and fibrotic potential observed in our *in vitro* and *in vivo* experiments. FLI1 in particular has been shown to suppress *Col1* expression, and in the context of Ewing sarcoma (a highly metastatic bone cancer), it disrupts YAP1/TEAD mechanotransduction.^{28,29}

Collectively, this study provides previously unappreciated insight into nuclear mechanics driving profibrotic liver myofibroblasts and highlights PAK1-dependent regulatory mechanisms linked to chromatin state as novel targetable areas for urgently needed therapeutic targets in fibrosis.

DISCUSSION

The cellular process underlying fibrosis in any organ is broadly similar.³⁰ In the liver, regardless of the source, failure to resolve liver injury leads to progressive fibrosis.³¹ Activated HSCs are widely regarded as the liver myofibroblasts responsible for tissue-damaging ECM deposition in fibrosis where the mechanical environment, in part, perpetuates this response.^{3,5,8,9} As a general principle, nuclear stiffness scales with tissue stiffness where brain cells, for example, would have a softer nucleus than bone.²⁵ However, the response of cells within an organ and at the multicellular level is likely to be more complex, particularly in disease states.

Tissue stiffness is a feature of fibrotic organs.^{8,9} Extent of scarring and stiffness in liver is a diagnostic determinant of disease severity.^{8,9,32} In light of this and previous studies, we might predict quiescent HSCs, as exist in normal healthy liver, to have a softer nucleus than activated HSCs, as exist in fibrotic liver. However, here, we discover that when HSCs encounter a stiffer environment, the nuclear response is to soften. Significantly, this is in parallel to a radical shift in cytoskeletal cell shape and profibrotic gene expression.

The reasons underlying this are likely 2-fold. First, profibrotic HSCs are contractile, migratory myofibroblasts, and as part of this phenotype, a malleable nucleus would promote their ability

to infiltrate the surrounding tissue and further deposit ECM. Second, although activated HSCs have been associated with promoting an environment conducive to cancer in end-stage cirrhosis,³³ HSCs themselves are not known to be associated with DNA damage. In keeping with studies in skin,²² nuclear softening would provide a protective mechanism and propagate the profibrotic response.

It is clear that the shift in cell shape from quiescent to activated HSCs, and increasingly profibrotic myofibroblasts in lung, is paralleled by a major change in the actin cytoskeleton.^{3,9–11,13,14} Through perturbing the actin cytoskeleton by *Pak1* loss, we highlight a functional mechano-response of liver myofibroblasts driven by nuclear deformation and H3K9Me3-mediated chromatin remodeling. These findings are consistent with a profound switch in profibrotic gene expression and one that further permits their migratory, contractile phenotype.

Interestingly, during liver development, loss of H3K9Me3 correlates with hepatocyte differentiation and maturation.³⁴ More broadly, although the role of H3K9Me3 in gene silencing is complex, a number of studies have indicated its increasingly important function in cell-type-specific chromatin organization and gene expression.^{21,34–36} H3K9Me3 is associated with condensed chromatin and restricted TF binding due to reduced accessibility of heterochromatic promoters.^{36–39} Similarly, in this study, using ATAC-seq, we demonstrated increased chromatin accessibility parallels loss of H3K9Me3. The correlation with enhanced nuclear adaptation, measured by AFM, and profibrotic gene expression as quiescent HSCs switch to an activated phenotype supports the idea that H3K9Me3 compacts chromatin structure and restricts gene expression programs. These data have similarities to other studies and support the idea that changes in H3K9Me3 deposition provide a distinct chromatin structural organization permissible to tissue-specific TF networks.^{21,34,36–39}

Linked to these findings, we also observed altered expression of lamin proteins, particularly lamin B, following impaired actin signaling. Aside from their structural properties as components of the inner NE, lamins are also associated with chromatin organization and gene expression through LADs.²⁰ Whether the relative composition of lamin proteins in HSCs also plays a role in creating permissible gene regulatory environments through their different expression and nucleoplasmic localization is unknown.

One central response for transmitting the cellular mechanical signals to the nucleus is the LINC complex.⁴⁰ Aside from their role and physical connection to the nuclear lamins and chromatin organization, LINC proteins provide a key morphological response to mechanical stimulation. For example, in the absence of the LINC complex protein nesprin 1 (NESP1), transmission of force to the nucleus in mechanically stretched endothelial cells was diminished, and nuclei exhibited a rounded, relaxed shape.⁴¹ Interestingly, HSCs transfected with a dominant-negative nesprin peptide to inhibit coupling of the nucleus with the cytoskeleton resulted in reduced nuclear deformation under stiff culture conditions, whereas no effect was observed on soft matrices.⁴² These data support our current study indicating the effect of matrix stiffness on the nuclear morphology of HSCs is dependent on cytoskeletal tension.

Ultimately, uncovering these mechanisms may provide insight into the 3D chromatin structure and fine control mechanisms of HSCs and transformation into profibrotic myofibroblasts. For cell-specific therapeutic targeting, a comprehensive understanding of external mechanical cues through signals that impact nuclear function seems critical to identifying pharmaceutical targets to block or reverse fibrosis.⁴³ As a first step to translation, we provide evidence that targeting actomyosin signaling during liver and lung fibrosis *in vivo* significantly reduces scarring and liver myofibroblast accumulation. However, our collective data also highlight H3K9Me3 as a potential therapeutic antifibrotic target in liver disease through modulation of methyltransferases (e.g., SUV39H1).⁴³ In other models of organ fibrosis, although not assessed in a cell-specific manner, increased levels of H3K9me3 have been highlighted in kidney fibrosis.⁴⁴ More interestingly, this study did show a more diffuse spatial distribution of H3K9me3 in response to TGF- β (the main profibrotic cytokine in organ fibrosis), which parallels our observation of chromatin decondensing during *in vitro* activation. Overall, given mechanisms underlying fibrosis are common across organs, our study and datasets have broad appeal across chronic disease where fibrosis is a progressive step to organ dysfunction.

Limitations of the study

Among this study's limitations is that the potential cause-effect relationship and the underlying mechanisms between chromatin condensation and contractility-induced (PAK1-dependent) changes in nuclear size remain to be elucidated. More specifically, limitations relate to *in vivo* interrogation of H3K9Me3 and nuclear size of HSCs directly in tissue during experimental fibrosis. In particular, the ability to show increased levels of H3K9Me3 in the quiescent state *in vivo* directly in tissue was challenging and limited by available markers to characterize true quiescent HSC state. Linking this (and PAK1 expression) with nuclear size *in vivo* during HSC activation and transitioning states was similarly limited. Although interesting observations were detected in response to PAK1 on lamin protein levels, in particular LMNB1, this was not interrogated further as part of this study. To fully understand the impact of LMNB1 would require integration of chromatin organization with chromatin capture techniques in profibrotic HSCs linked to animal models of *Lmnb1* loss for physiological understanding in fibrotic disease. Finally, the data presented here focused on transcript levels and fibrosis-relevant gene activation downstream of PAK1 loss rather than a broad analysis of target protein phosphorylation status as a result of PAK1 activity. Critically, this would also incorporate aspects of the LINC complex. These are both important and interesting areas of research that require further independent investigation with *in vitro* and *in vivo* modeling in fibrosis.

STAR★METHODS

Detailed methods are provided in the online version of this paper and include the following:

- KEY RESOURCES TABLE
- RESOURCE AVAILABILITY
 - Lead contact

- Materials availability
- Data and code availability
- EXPERIMENTAL MODEL AND STUDY PARTICIPANT DETAILS
 - Animals
 - Cell lines
 - Primary cell culture
 - Clinical samples
- METHOD DETAILS
 - Primary cell isolation and cell culture
 - Animal models of fibrosis
 - siRNA knockdown
 - Immunoblotting and quantitative RT-PCR
 - Histology, immunohistochemistry and RNAScope
 - Immunofluorescence, micropatterns and nuclear morphology analyses
 - Live F-actin, contraction and cell migration
 - Atomic force microscopy (AFM)
 - RNA microarray
 - Cut&Tag
 - ATAC-seq/RNA-seq
- QUANTIFICATION AND STATISTICAL ANALYSIS

SUPPLEMENTAL INFORMATION

Supplemental information can be found online at <https://doi.org/10.1016/j.celrep.2023.113414>.

ACKNOWLEDGMENTS

This work was supported by the Medical Research Council (MRC; K.P.H., MR/J003352/1 and MR/P023541/1; N.A.H., MR/000638/1 and MR/S036121/1; and K.M. and V.S.A. are MRC Clinical Training Fellows). We thank Sara Wickstrom and her team at the University of Helsinki for technical and experimental guidance. The Genomics Core Facility and the Bioimaging Facility at the University of Manchester are acknowledged for their technical help and support from Wellcome (105610). K.P.H. is a member of the Wellcome Trust supported Centre for Cell-Matrix Research (203128/Z/16/Z). This report is independent research supported by the North West Lung Center Charity at Manchester University NHS Foundation Trust. The authors would like to acknowledge the Manchester Allergy, Respiratory and Thoracic Surgery Biobank and the North West Lung Center Charity for supporting this project. The views expressed in this publication are those of the author(s) and not necessarily those of the NHS, the North West Lung Center Charity, or the Department of Health. The graphical abstract was prepared using [BioRender.com](https://www.biorender.com).

AUTHOR CONTRIBUTIONS

K.P.H. conceived and designed experiments. E.J., A.F.M., K.M., N.W.H., C.J.W., and N.A.H. contributed to experimental design. E.J., A.F.M., K.S., L.B., L.P., K.M., J.P., N.W.H., C.J.W., and V.S.A. performed experiments. V.S.A. and R.S. provided human tissues. E.J., A.F.M., E.C., S.R., L.Z., and K.P.H. analyzed the data. L.Z. and I.D. performed bioinformatics. E.C. carried out complex statistics. K.P.H. and E.J. guided experiments and wrote the manuscript.

DECLARATION OF INTERESTS

The authors declare no competing financial interests.

INCLUSION AND DIVERSITY

We support inclusive, diverse, and equitable conduct of research.

Received: March 14, 2023
Revised: September 14, 2023
Accepted: October 25, 2023
Published: November 14, 2023

REFERENCES

1. Iwaisako, K., Jiang, C., Zhang, M., Cong, M., Moore-Morris, T.J., Park, T.J., Liu, X., Xu, J., Wang, P., Paik, Y.H., et al. (2014). Origin of myofibroblasts in the fibrotic liver in mice. *Proc. Natl. Acad. Sci. USA* *111*, E3297–E3305.
2. Lemoine, S., Cadoret, A., El Mourabit, H., Thabut, D., and Housset, C. (2013). Origins and functions of liver myofibroblasts. *Biochim. Biophys. Acta* *1832*, 948–954.
3. Martin, K., Pritchett, J., Llewellyn, J., Mullan, A.F., Athwal, V.S., Dobie, R., Harvey, E., Zeef, L., Farrow, S., Streuli, C., et al. (2016). PAK proteins and YAP-1 signalling downstream of integrin beta-1 in myofibroblasts promote liver fibrosis. *Nat. Commun.* *7*, 12502.
4. Mederacke, I., Hsu, C.C., Troeger, J.S., Huebener, P., Mu, X., Dapito, D.H., Pradere, J.P., and Schwabe, R.F. (2013). Fate tracing reveals hepatic stellate cells as dominant contributors to liver fibrosis independent of its aetiology. *Nat. Commun.* *4*, 2823.
5. Tsuchida, T., and Friedman, S.L. (2017). Mechanisms of hepatic stellate cell activation. *Nat. Rev. Gastroenterol. Hepatol.* *14*, 397–411.
6. Caliari, S.R., Perepeyuk, M., Cosgrove, B.D., Tsai, S.J., Lee, G.Y., Mauck, R.L., Wells, R.G., and Burdick, J.A. (2016). Stiffening hydrogels for investigating the dynamics of hepatic stellate cell mechanotransduction during myofibroblast activation. *Sci. Rep.* *6*, 21387.
7. Schuppan, D., Ruehl, M., Somasundaram, R., and Hahn, E.G. (2001). Matrix as a modulator of hepatic fibrogenesis. *Semin. Liver Dis.* *21*, 351–372.
8. Wells, R.G. (2008). The role of matrix stiffness in regulating cell behavior. *Hepatology* *47*, 1394–1400.
9. Athwal, V.S., Pritchett, J., Llewellyn, J., Martin, K., Camacho, E., Raza, S.M., Phythian-Adams, A., Birchall, L.J., Mullan, A.F., Su, K., et al. (2017). SOX9 predicts progression toward cirrhosis in patients while its loss protects against liver fibrosis. *EMBO Mol. Med.* *9*, 1696–1710.
10. Athwal, V.S., Pritchett, J., Martin, K., Llewellyn, J., Scott, J., Harvey, E., Zaitoun, A.M., Mullan, A.F., Zeef, L.A.H., Friedman, S.L., et al. (2018). SOX9 regulated matrix proteins are increased in patients serum and correlate with severity of liver fibrosis. *Sci. Rep.* *8*, 17905.
11. Hanley, K.P., Oakley, F., Sugden, S., Wilson, D.I., Mann, D.A., and Hanley, N.A. (2008). Ectopic SOX9 mediates extracellular matrix deposition characteristic of organ fibrosis. *J. Biol. Chem.* *283*, 14063–14071.
12. Pritchett, J., Athwal, V., Roberts, N., Hanley, N.A., and Hanley, K.P. (2011). Understanding the role of SOX9 in acquired diseases: lessons from development. *Trends Mol. Med.* *17*, 166–174.
13. Pritchett, J., Athwal, V.S., Harvey, E., Martin, K., Llewellyn, J., Ireland, P., Nicolaides, A., Humphries, M.J., Bobola, N., Hanley, N.A., and Piper Hanley, K. (2014). Epimorphin alters the inhibitory effects of SOX9 on Mmp13 in activated hepatic stellate cells. *PLoS One* *9*, e100091.
14. Pritchett, J., Harvey, E., Athwal, V., Berry, A., Rowe, C., Oakley, F., Moles, A., Mann, D.A., Bobola, N., Sharrocks, A.D., et al. (2012). Osteopontin is a novel downstream target of SOX9 with diagnostic implications for progression of liver fibrosis in humans. *Hepatology* *56*, 1108–1116.
15. Henderson, N.C., Arnold, T.D., Katamura, Y., Giacomini, M.M., Rodriguez, J.D., McCarty, J.H., Pellicoro, A., Raschperger, E., Betsholtz, C., Ruminski, P.G., et al. (2013). Targeting of alpha_v integrin identifies a core molecular pathway that regulates fibrosis in several organs. *Nat. Med.* *19*, 1617–1624.
16. Aureille, J., Belaadi, N., and Guilly, C. (2017). Mechanotransduction via the nuclear envelope: a distant reflection of the cell surface. *Curr. Opin. Cell Biol.* *44*, 59–67.
17. Belaadi, N., Aureille, J., and Guilly, C. (2016). Under Pressure: Mechanical Stress Management in the Nucleus. *Cells* *5*, 27.
18. Le, H.Q., Ghatak, S., Yeung, C.Y.C., Tellkamp, F., Günschmann, C., Dietrich, C., Yeroslaviz, A., Habermann, B., Pombo, A., Niessen, C.M., and Wickström, S.A. (2016). Mechanical regulation of transcription controls Polycomb-mediated gene silencing during lineage commitment. *Nat. Cell Biol.* *18*, 864–875.
19. Crisp, M., Liu, Q., Roux, K., Rattner, J.B., Shanahan, C., Burke, B., Stahl, P.D., and Hodzic, D. (2006). Coupling of the nucleus and cytoplasm: role of the LINC complex. *J. Cell Biol.* *172*, 41–53.
20. van Steensel, B., and Belmont, A.S. (2017). Lamina-Associated Domains: Links with Chromosome Architecture, Heterochromatin, and Gene Repression. *Cell* *169*, 780–791.
21. Nicetto, D., and Zaret, K.S. (2019). Role of H3K9me3 heterochromatin in cell identity establishment and maintenance. *Curr. Opin. Genet. Dev.* *55*, 1–10.
22. Nava, M.M., Miroshnikova, Y.A., Biggs, L.C., Whitefield, D.B., Metge, F., Boucas, J., Vihinen, H., Jokitalo, E., Li, X., Garcia Arcos, J.M., et al. (2020). Heterochromatin-Driven Nuclear Softening Protects the Genome against Mechanical Stress-Induced Damage. *Cell* *181*, 800–817.e22.
23. Sabra, H., Brunner, M., Mandati, V., Wehrle-Haller, B., Lallemand, D., Ribba, A.S., Chevalier, G., Guardiola, P., Block, M.R., and Bouvard, D. (2017). beta1 integrin-dependent Rac/group I PAK signaling mediates YAP activation of Yes-associated protein 1 (YAP1) via NF2/merlin. *J. Biol. Chem.* *292*, 19179–19197.
24. Gruenbaum, Y., and Foisner, R. (2015). Lamins: nuclear intermediate filament proteins with fundamental functions in nuclear mechanics and genome regulation. *Annu. Rev. Biochem.* *84*, 131–164.
25. Swift, J., Ivanovska, I.L., Buxboim, A., Harada, T., Dingal, P.C.D.P., Pinter, J., Pajeroski, J.D., Spinler, K.R., Shin, J.W., Tewari, M., et al. (2013). Nuclear lamin-A scales with tissue stiffness and enhances matrix-directed differentiation. *Science* *341*, 1240104.
26. Dobie, R., Wilson-Kanamori, J.R., Henderson, B.E.P., Smith, J.R., Matchett, K.P., Portman, J.R., Wallenborg, K., Picelli, S., Zagorska, A., Pendem, S.V., et al. (2019). Single-Cell Transcriptomics Uncovers Zonation of Function in the Mesenchyme during Liver Fibrosis. *Cell Rep.* *29*, 1832–1847.e8.
27. Ramachandran, P., Dobie, R., Wilson-Kanamori, J.R., Dora, E.F., Henderson, B.E.P., Luu, N.T., Portman, J.R., Matchett, K.P., Brice, M., Marwick, J.A., et al. (2019). Resolving the fibrotic niche of human liver cirrhosis at single-cell level. *Nature* *575*, 512–518.
28. Katschnig, A.M., Kauer, M.O., Schwentner, R., Tomazou, E.M., Mutz, C.N., Linder, M., Sibilja, M., Alonso, J., Aryee, D.N.T., and Kovar, H. (2017). EWS-FLI1 perturbs MRTFB/YAP-1/TEAD target gene regulation inhibiting cytoskeletal autoregulatory feedback in Ewing sarcoma. *Oncogene* *36*, 5995–6005.
29. Wang, Y., Fan, P.S., and Kahaleh, B. (2006). Association between enhanced type I collagen expression and epigenetic repression of the FLI1 gene in scleroderma fibroblasts. *Arthritis Rheum.* *54*, 2271–2279.
30. Rockey, D.C., Bell, P.D., and Hill, J.A. (2015). Fibrosis—A Common Pathway to Organ Injury and Failure. *N. Engl. J. Med.* *373*, 96.
31. Williams, R., Alexander, G., Armstrong, I., Baker, A., Bhalra, N., Camps-Walsh, G., Cramp, M.E., de Lusignan, S., Day, N., Dhawan, A., et al. (2018). Disease burden and costs from excess alcohol consumption, obesity, and viral hepatitis: fourth report of the Lancet Standing Commission on Liver Disease in the UK. *Lancet* *391*, 1097–1107.
32. Ganne-Carrié, N., Ziol, M., de Ledinghen, V., Douvin, C., Marcellin, P., Castera, L., Dhumeaux, D., Trinchet, J.C., and Beaugrand, M. (2006). Accuracy of liver stiffness measurement for the diagnosis of cirrhosis in patients with chronic liver diseases. *Hepatology* *44*, 1511–1517.
33. Barry, A.E., Baldeosingh, R., Lamm, R., Patel, K., Zhang, K., Dominguez, D.A., Kirton, K.J., Shah, A.P., and Dang, H. (2020). Hepatic Stellate Cells and Hepatocarcinogenesis. *Front. Cell Dev. Biol.* *8*, 709.
34. Nicetto, D., Donahue, G., Jain, T., Peng, T., Sidoli, S., Sheng, L., Montavon, T., Becker, J.S., Grindheim, J.M., Blahnik, K., et al. (2019).

- H3K9me3-heterochromatin loss at protein-coding genes enables developmental lineage specification. *Science* 363, 294–297.
35. Feng, Y., Wang, Y., Wang, X., He, X., Yang, C., Naseri, A., Pederson, T., Zheng, J., Zhang, S., Xiao, X., et al. (2020). Simultaneous epigenetic perturbation and genome imaging reveal distinct roles of H3K9me3 in chromatin architecture and transcription. *Genome Biol.* 21, 296.
 36. Methot, S.P., Padeken, J., Brancati, G., Zeller, P., Delaney, C.E., Gaidatzis, D., Kohler, H., van Oudenaarden, A., GroBhans, H., and Gasser, S.M. (2021). H3K9me selectively blocks transcription factor activity and ensures differentiated tissue integrity. *Nat. Cell Biol.* 23, 1163–1175.
 37. Becker, J.S., McCarthy, R.L., Sidoli, S., Donahue, G., Kaeding, K.E., He, Z., Lin, S., Garcia, B.A., and Zaret, K.S. (2017). Genomic and Proteomic Resolution of Heterochromatin and Its Restriction of Alternate Fate Genes. *Mol. Cell* 68, 1023–1037.e15.
 38. Llères, D., Bailly, A.P., Perrin, A., Norman, D.G., Xirodimas, D.P., and Feil, R. (2017). Quantitative FLIM-FRET Microscopy to Monitor Nanoscale Chromatin Compaction In Vivo Reveals Structural Roles of Condensin Complexes. *Cell Rep.* 18, 1791–1803.
 39. Rea, S., Eisenhaber, F., O'Carroll, D., Strahl, B.D., Sun, Z.W., Schmid, M., Opravil, S., Mechtler, K., Ponting, C.P., Allis, C.D., and Jenuwein, T. (2000). Regulation of chromatin structure by site-specific histone H3 methyltransferases. *Nature* 406, 593–599.
 40. Khilan, A.A., Al-Maslami, N.A., and Horn, H.F. (2021). Cell stretchers and the LINC complex in mechanotransduction. *Arch. Biochem. Biophys.* 702, 108829.
 41. Anno, T., Sakamoto, N., and Sato, M. (2012). Role of nesprin-1 in nuclear deformation in endothelial cells under static and uniaxial stretching conditions. *Biochem. Biophys. Res. Commun.* 424, 94–99.
 42. Guixé-Muntet, S., Ortega-Ribera, M., Wang, C., Selicean, S., Andreu, I., Kechagia, J.Z., Fondevila, C., Roca-Cusachs, P., Dufour, J.F., Bosch, J., et al. (2020). Nuclear deformation mediates liver cell mechanosensing in cirrhosis. *JHEP Rep.* 2, 100145.
 43. Van, M.V., Fujimori, T., and Bintu, L. (2021). Nanobody-mediated control of gene expression and epigenetic memory. *Nat. Commun.* 12, 537.
 44. Hewitson, T.D., Holt, S.G., Tan, S.J., Wigg, B., Samuel, C.S., and Smith, E.R. (2017). Epigenetic Modifications to H3K9 in Renal Tubulointerstitial Cells after Unilateral Ureteric Obstruction and TGF-beta1 Stimulation. *Front. Pharmacol.* 8, 307.
 45. Allen, J.D., Jaffer, Z.M., Park, S.J., Burgin, S., Hofmann, C., Sells, M.A., Chen, S., Derr-Yellin, E., Michels, E.G., McDaniel, A., et al. (2009). p21-activated kinase regulates mast cell degranulation via effects on calcium mobilization and cytoskeletal dynamics. *Blood* 113, 2695–2705.
 46. Raza, S., Jokl, E., Pritchett, J., Martin, K., Su, K., Simpson, K., Birchall, L., Mullan, A.F., Athwal, V.S., Doherty, D.T., et al. (2021). SOX9 is required for kidney fibrosis and activates NAV3 to drive renal myofibroblast function. *Sci. Signal.* 14, eabb4282.
 47. Bolger, A.M., Lohse, M., and Usadel, B. (2014). Trimmomatic: a flexible trimmer for Illumina sequence data. *Bioinformatics* 30, 2114–2120.
 48. Mouse Genome Sequencing Consortium; Waterston, R.H., Lindblad-Toh, K., Birney, E., Rogers, J., Abril, J.F., Agarwal, P., Agarwala, R., Ainscough, R., Alexandersson, M., et al. (2002). Initial sequencing and comparative analysis of the mouse genome. *Nature* 420, 520–562.
 49. Langmead, B., and Salzberg, S.L. (2012). Fast gapped-read alignment with Bowtie 2. *Nat. Methods* 9, 357–359.
 50. Li, H., Handsaker, B., Wysoker, A., Fennell, T., Ruan, J., Homer, N., Marth, G., Abecasis, G., and Durbin, R.; 1000 Genome Project Data Processing Subgroup (2009). The Sequence Alignment/Map format and SAMtools. *Bioinformatics* 25, 2078–2079.
 51. Quinlan, A.R., and Hall, I.M. (2010). BEDTools: a flexible suite of utilities for comparing genomic features. *Bioinformatics* 26, 841–842.
 52. Meers, M.P., Tenenbaum, D., and Henikoff, S. (2019). Peak calling by Sparse Enrichment Analysis for CUT&RUN chromatin profiling. *Epigenet. Chromatin* 12, 42.
 53. Ou, J., Liu, H., Yu, J., Kelliher, M.A., Castilla, L.H., Lawson, N.D., and Zhu, L.J. (2018). ATACseqQC: a Bioconductor package for post-alignment quality assessment of ATAC-seq data. *BMC Genom.* 19, 169.
 54. Zhang, Y., Liu, T., Meyer, C.A., Eeckhoutte, J., Johnson, D.S., Bernstein, B.E., Nussbaum, C., Myers, R.M., Brown, M., Li, W., and Liu, X.S. (2008). Model-based analysis of ChIP-Seq (MACS). *Genome Biol.* 9, R137.
 55. Stark, R., and Brown, G. (2011). DiffBind: Differential Binding Analysis of ChIP-Seq Peak Data. <http://bioconductor.org/packages/release/bioc/vignettes/DiffBind/inst/doc/DiffBind.pdf>.
 56. Xie, Z., Bailey, A., Kuleshov, M.V., Clarke, D.J.B., Evangelista, J.E., Jenkins, S.L., Lachmann, A., Wojciechowicz, M.L., Kropiwnicki, E., Jagodnik, K.M., et al. (2021). Gene Set Knowledge Discovery with Enrichr. *Curr. Protoc.* 1, e90.
 57. Bailey, T., and Grant, C.S.E.A. (2021). Simple Enrichment Analysis of motifs. Preprint at bioRxiv. <https://doi.org/10.1101/2021.08.23.457422>.

STAR★METHODS

KEY RESOURCES TABLE

REAGENT or RESOURCE	SOURCE	IDENTIFIER
Antibodies		
anti-ITGB1	Millipore	Cat# MAB1997; RRID: AB_2128202
anti- α SMA	Leica Biosystems	Cat# NCL-L-SMA; RRID: AB_442134
anti-COL1	Southern Biotech	Cat# 1310-01; RRID: AB_2753206
anti-SOX9	Millipore	Cat# AB5535; RRID: AB_2239761
anti-MYL9	Cell Signaling Technologies	Cat# 3762; RRID: AB_10692513
anti-YAP	Santa Cruz Biotechnology	Cat# Sc-271134; RRID: AB_10612397
anti-pMYL9	Cell Signaling Technologies	Cat# 3671P; RRID: AB_330248
anti-PAK1	Cell Signaling Technologies	Cat# 2602; RRID: AB_330222
anti-pPAK1/2	Cell Signaling Technologies	Cat# 2606; RRID: AB_2299279
anti-ITGA11	R&D Systems	Cat# MAB4235; RRID: AB_2129095
anti-FAK	Cell Signaling Technologies	Cat# 3285; RRID: AB_2269034
anti-pNF2	Cell Signaling Technologies	Cat# 9163; RRID: AB_2149793
anti-NF2	Atlas Antibodies	Cat# HPA003097; RRID: AB_1079473
anti-LMNA/C	Cell Signaling Technologies	Cat# 2032; RRID: AB_2136278
anti-LMNB1	Santa Cruz Biotechnology	Cat# 374015; RRID: AB_10947408
anti-H3K9Me3	Cell Signaling Technologies	Cat# 13969; RRID: AB_2798355
anti-SUV39H1	Cell Signaling Technologies	Cat# 8729; RRID: AB_10829612
anti-SETDB1	Abcam	Cat# ab12317; RRID: AB_299005
anti- β actin HRP	Sigma	Cat# A3854; RRID: AB_262011
anti-Vimentin	Abcam	Cat# ab24525; RRID: AB_778824
anti-H3K9Me3	Active Motif	Cat# 39765; RRID: AB_2793334
anti-CK19	Abcam	Cat# ab52625; RRID: AB_2281020
anti-rabbit HRP	Thermo Fisher Scientific	Cat# 31460; RRID: AB_228341
anti-goat HRP	Abcam	Cat# ab97100; RRID: AB_10687752
anti-mouse HRP	Cell Signaling Technologies	Cat# 58802; RRID: AB_2799549
anti-rabbit 488	Thermo Fisher Scientific	Cat# A-32731; RRID: AB_2633280
anti-rabbit 594	Thermo Fisher Scientific	Cat# A-11012; RRID: AB_2534079
anti-mouse 488	Thermo Fisher Scientific	Cat# A-11001; RRID: AB_2534069
anti-mouse 594	Thermo Fisher Scientific	Cat# A-11005; RRID: AB_2534073
Biological samples		
Human liver tissue	Manchester Foundation Trust Biobank	REC 14/NW1260/22
Human lung sections	ManARTS Biobank	REC 20/NW/0302; M2014-18
Chemicals, peptides, and recombinant proteins		
Blebbistatin	Tocris	Cat# 1760
1-Oleoyl lysophosphatidic acid (LPA)	Tocris	Cat# 3854
Collagenase B	Roche	Cat# 11088815
Pronase	Roche	Cat# 10165921
DNase	Roche	Cat# 11284932
Phalloidin-488	Thermo Fisher Scientific	Cat# A12379
SiR-actin	Cytoskeleton Inc.	Cat# CY-SC001

(Continued on next page)

Continued		
REAGENT or RESOURCE	SOURCE	IDENTIFIER
Critical commercial assays		
Complete CUT&Tag Assay Kit	Active Motif	Cat# 53160
Deposited data		
RNA-seq data	This study	ArrayExpress: E-MTAB-12909
ATAC-seq data	This study	ArrayExpress: E-MTAB-12908
Cut&Tag data	This study	ArrayExpress: E-MTAB-12907
Experimental models: Cell lines		
LX2 Cell line	Gifted by Prof. S Friedman	N/A
Experimental models: Organisms/strains		
Mouse: Pak1-null	gifted by Dr Solaro (University of Illinois) and Dr Chernoff (Fox Chase Center, Philadelphia)	N/A
Mouse: FVB	ENVIGO	FVB
Oligonucleotides		
DNA Oligonucleotides	This paper, see Table S6 for sequences	N/A
Software and algorithms		
Graphpad Prism 9	Graphpad Software	https://www.graphpad.com/scientific-software/prism/
ImageJ	NIH	https://imagej.nih.gov/ij/index.html
SlideBook 6	Intelligent Imaging	https://www.intelligent-imaging.com/slidebook
Adobe Photoshop	Adobe	https://www.adobe.com/uk/products/photoshop.html
NIS-Elements AR	Nikon	https://www.microscope.healthcare.nikon.com/
JPK Data Analysis	JPK	https://www.tableau.com/products

RESOURCE AVAILABILITY

Lead contact

Requests for further information or resources should be directed to Prof. Karen Piper Hanley (Karen.piperhanley@manchester.ac.uk).

Materials availability

This study did not generate new, unique reagents.

Data and code availability

- RNA-seq, ATAC-seq and Cut&TAG datasets have been deposited at ArrayExpress and are publicly available with the accession numbers MTAB-12909, MTAB-12908, MTAB-12907 respectively. Also see [Key resources table](#). The original full-western blots for [Figures 4E](#) and [4F](#), [5E](#), [5F](#), [6A](#), [6B](#), [6E](#), [6G](#), [S1A](#), [S1C](#), and [S2D](#) have been collated in [Figures S8–S11](#). Other data reported in this paper will be shared by the [lead contact](#) upon request
- No original code was generated for this study.
- Any additional information required to reanalyze the data reported in this paper is available from the [lead contact](#) upon request.

EXPERIMENTAL MODEL AND STUDY PARTICIPANT DETAILS

Animals

The *Pak1*-null mice were developed by Dr Chernoff (Fox Chase Center, Philadelphia) and gifted by Dr Solaro (University of Illinois) and Dr Chernoff.⁴⁵ Animals are from the FVB genetic background. Animals were genotyped by PCR with a 280bp wild-type product detected with forward 5'-GCCCTTCACAGGAGCTTAATGA-3' and reverse 5'-GAAAGGACTGAATCTAATAGCA-3' and a 360bp *Pak1*-null product detected using the same forward primer and reverse 5'-CATTTGTACAGTCTGCACGA-3'. Animals were housed, maintained, and experiments performed in accordance to UK Government Home Office regulations and under approval from the University of Manchester Ethical Review Committee. Fibrosis models were performed on 8–12 week old male mice. The use of only male mice may limit the generalizability of these studies.

Cell lines

The LX2 immortalised human hepatic stellate cell line was gifted by Prof. Scott Friedman (Mount Sinai School of Medicine, New York). LX2 cells originate from a male donor, thus the studies performed may not be fully generalizable.

Primary cell culture

Primary hepatic stellate cells were isolated as described in the [methods details](#) section below. Mice were age (10–15 weeks) and gender (male) matched. The use of only male mice may limit the generalizability of these studies.

Clinical samples

Liver tissues were obtained with informed consent and ethical approval (National Research Ethics Service, REC 14/NW1260/22) from the Manchester Foundation Trust Biobank. Human lung sections were obtained following informed consent and ethical approval (National Research Ethics Service, REC 20/NW/0302) from the Manchester Allergy, Respiratory and Thoracic Surgery (ManARTS) Biobank (study number M2014-18).

METHOD DETAILS

Primary cell isolation and cell culture

Mouse hepatic stellate cells (HSCs) were isolated as previously described.^{3,9,11} Briefly, livers were perfused with HBSS containing collagenase and pronase via the portal vein prior to mechanical disruption of tissue and isolation of HSCs via an Optiprep density gradient (Sigma). Cells were cultured in high glucose DMEM enriched with L-glutamine, pen-strep and 16% serum. Mouse lung fibroblasts were isolated by incubating lung tissue minced using razor blades in a collagenase/pronase solution at 37° for approximately 1 h with periodic agitation, followed by straining through a 40 μ m filter, pelleting at 4° at 800g for 5 min and resuspension in high glucose DMEM enriched with L-glutamine, pen-strep and 10% serum before plating. LX2 cells were maintained in high glucose DMEM enriched with L-glutamine, pen-strep and 10% serum.

Blebbistatin (#1760, Tocris) or an equivalent volume of DMSO was added to culture media at a final concentration of 50 μ M for 2 h prior to cell fixation. 1-Oleoyl lysophosphatidic acid (LPA #3854, Tocris) or an equivalent volume of PBS was added at a final concentration of 50 μ M 24 h prior to cell fixation.

Animal models of fibrosis

Bile Duct Ligation (BDL) and carbon tetrachloride (CCl₄) models of fibrosis were performed as previously described on *Pak1*-null and WT (FVB) control animals.^{3,9} CCl₄ was administered twice weekly by intraperitoneal (i.p.) injections of 2 μ L per g body weight CCl₄ (Sigma) at ratio of 1:3 by volume in olive oil (Sigma) or olive oil alone (control) twice weekly for 8 weeks. BDL was carried out under anesthesia using two ligatures to ligate the bile duct. Sham-operated mice underwent the same procedure but without tying the ligatures. BDL mice developed cholestasis and associated fibrosis over a 14-day period. For bleomycin induced lung fibrosis, 2.5IU per kg body weight of bleomycin in saline, or an equivalent volume of saline alone, was delivered by intratracheal administration under anesthesia. These mice developed lung fibrosis over a 21 day period.

At the end of these experiments, animals were sacrificed, blood taken for liver function biochemistry, liver and body weight recorded and tissues processed for histology.

Isolation of *in vivo* activated HSCs was performed as previously described.³ *Pak1*-null and FVB animals were injected with 2 μ L per g body weight CCl₄ at ratio of 1:3 by volume in olive oil every two days for a total of 4 doses. Isolation of *in vivo* activated HSCs was performed 24h after the final CCl₄ dose.

siRNA knockdown

SUV39H1 and *SETDB1* genes were targeted simultaneously with FlexiTube GeneSolution siRNA (Qiagen). Two independent siRNA pools were generated, each containing a pair of siRNAs against each gene: pool 1 (Hs_SETDB1_2, Hs_SETDB1_7, Hs_SUV39H1_1, Hs_SUV39H1_2) and pool 2 (Hs_SETDB1_8, Hs_SETDB1_9, Hs_SUV39H1_4, Hs_SUV39H1_7). siRNAs, or an equivalent amount of AllStars negative control siRNA (Qiagen), were transfected into LX2 cells using Lipofectamine 3000 transfection reagent as per manufacturer's instructions. Cells were harvested at 48hrs post transfection prior to RNA extraction and qPCR analysis as described below.

Immunoblotting and quantitative RT-PCR

Protein from cells and tissues was extracted in RIPA buffer and expression levels determined by a standard western blotting protocol using antibodies with total protein on the transfer blot or B-actin used as a loading control as indicated in the main text. The following primary and secondary antibodies were used: anti-ITGB1 (MAB1997, Millipore, dilution: 1:1000), anti- α -SMA (NCL-L-SMA, Leica Biosystems, 1:500), anti-COL1 (1310-01, Southern Biotech, 1:1000), anti-SOX9 (AB5535, Millipore, 1:5000), anti-MYL9 (3672, Cell Signaling, 1:500), anti-YAP (Sc-271134, Santa Cruz, 1:1000), anti-PMYL9 (#3671P, Cell Signaling, 1:500), anti-PAK1 (#2602, Cell Signaling, 1:1000), anti-phospho-PAK1/2 (#2606, Cell Signaling, 1:250) anti-ITGA11 (MAB4235, R & D Systems, 1:500), anti-FAK (CST/3285, Cell Signaling, 1:1000), anti-PNF2 (CST/9163, Cell Signaling, 1:500), anti-NF2 (HPA003097, Atlas, 1:500), anti-LMNA/C (CST/2032, Cell Signaling, 1:1000), anti-LMNB1 (374015, Santa Cruz, 1:1000), anti-H3K9Me3 (CST/13969, 1:1000), anti-SUV39H1 (CST/8729, Cell Signaling, 1:500), anti-SETDB1 (ab12317, Abcam, 1:1000), anti- β -actin HRP conjugate (A3854, Sigma, 1:50000) and species-specific HRP conjugated secondary antibodies (GE Healthcare).

RNA was extracted using a RNeasy purification kit (Qiagen) followed by cDNA conversion using High Capacity RNA-to-cDNA kit (Life Technologies). Relative transcript abundance was determined using the $\Delta\Delta C_T$ method in an SYBR Green assay with GusB and ActinB used in combination for normalisation to housekeeping genes. Primer sequences can be found in Table S6.

Histology, immunohistochemistry and RNAScope

Samples for histology were fixed in 4% PFA overnight followed by storage in 70% ethanol prior to embedding in paraffin and sectioning at 5 μ m thickness. Histological staining and quantification was performed as previously described.^{3,9} All livers were embedded in an identical orientation and corresponding histology images within the manuscript are shown from the same liver lobe. The extent of scarring was assessed in livers using picro-sirius red (PSR) staining (Sigma). Immunohistochemistry for α -SMA (NCL-L-SMA, Leica Biosystems, dilution: 1:100) and CK19 (ab52625, Abcam, 1:500) was detected using diaminobenzidine (DAB) and Impact Vector Red (Vector Laboratories) respectively, counterstained with toluidine blue.

In situ hybridization for *Pak1* was performed using an RNAScope 2.5 LS Reagent Kit-RED kit (Cat. No.322150) according to manufacturer's instructions using a Leica Bond RX automated staining system.^{9,46} After baking and de-waxing slides for 15 min, they were pre-treated with HIER for 15 min at 95° and 15 min of protease digestion. After washing slides with the BOND wash solution (Leica), slides were incubated with *Pak1* RNA probes for 2 h. Detection of the probes was performed through the BOND polymer Refine Red Detection and haematoxylin kit (DS9390, Leica Bond). Haematoxylin (blue) was used as a counterstain. Slides were heat dried for 30 min at 60°. Following a single dip in pure xylene, slides were mounted (EcoMount, Biocare Medical) and cover-slipped. Quantification of RNAScope was performed using the scoring system in the manufacturer's instructions. Puncta were counted in 20 fields of view across three lobes per animal, with images centered on portal triads for consistency.

Quantification of PSR and α -SMA and CK19 staining was determined by morphometric analysis from images acquired using the 3D Hitech Panoramic 250 Flash II slide scanner. From all three lobes of the liver (100 \times total magnification), 10 regions were selected at random, and analyzed using Adobe Photoshop. The Color Range tool was used to select stained pixels (red for PSR, brown for α -SMA and red for CK19); the number of selected pixels was recorded and expressed as a fraction of the total number of pixels, averaged across the 10 different regions per section. All quantification was carried out blinded, without prior knowledge of sections or treatment/control group.

Immunofluorescence, micropatterns and nuclear morphology analyses

Isolated WT and *Pak1*-null HSCs were plated onto chamber slides or hydrogels to activate. Hydrogels of the indicated stiffness (Softwell plates, Cell Guidance Systems) were coated with fibronectin prior to seeding to ensure cell attachment. For micropattern analysis, cells were cultured on plastic for 5 days for activation before trypsinisation and plating onto fibronectin coated micropatterned coverslips (Cyto), proceeding to fixation 30 min after plating to allow adhesion and shape changes. At the indicated time point, media was removed, cells were washed twice in PBS and fixed in 4% PFA in PBS for 10 min. After 2 further PBS washes cells were stored under PBS at 4° until staining. Cells were stained with Alexa Fluor 488 phalloidin (Invitrogen 1:500) and/or the respective primary and secondary antibodies in a standard immunofluorescence protocol. Antibodies used were: anti-H3K9Me3 (#13969, CST, 1:500), anti- α -SMA (NCL-L-SMA, Leica, 1:100), anti-SOX9 (ab5535, Merck, 1:1000), anti-YAP (#4912, CST, 1:100), anti-LMNA/C (#2032, CST, 1:500), anti-Vimentin (ab24525, Abcam, 1:500) with their respective species specific Alexa Fluor conjugated secondary antibodies (Invitrogen 1:500). Cells were mounted in Vectashield +DAPI to visualise the nucleus. Images were collected on a Zeiss Axioimager D2 upright microscope and captured using a Coolsnap HQ2 camera (Photometrics) through Micromanager software v1.4.23.

For nuclear morphology analysis, In FIJI images from the DAPI channel were thresholded using the Image>Adjust>Threshold tool using a consistent value across images to define the nuclear area. These areas were saved as an overlay using the ROI manager. The overlay was applied to the original DAPI image to demarcate the nuclei and the nuclear areas were measured to provide average signal intensity and nuclear morphology data.

To identify the localisation of YAP protein in immunofluorescent stained hydrogels, the level of cytoplasmic and nuclear staining was measured and calculated as a ratio in (ImageJ) using the macro 'Intensity_Ratio_Nuclei_Cytoplasm'. Briefly, the DAPI channel was overlaid onto the YAP channel to define the nuclear area. The macro then calculated the relative intensity of YAP signal within and outside of the nuclear area. 20–30 cells per animal were analyzed.

Live F-actin, contraction and cell migration

To visualise live F-actin, WT and *Pak1*-null HSCs were plated at a density of 15,000 cells per well and incubated at 37°C in a glass-bottomed 24-well plate (Cellvis, USA). SiR-actin and Verapamil (Cytoskeleton Inc., USA) were added to cell media at a concentration of 1 μ L/mL and incubated for a minimum of 6 h at 37°C. Ten images per animal were taken at \times 20 magnification using a 3i spinning disc confocal microscope (Leica) and SlideBook 6 software (Intelligent Imaging, USA). Saturated SiR-actin fluorescence was quantified using color detection analysis in Photoshop software. The background in each image was deducted and saturated SiR-actin staining was calculated as a percentage of the remaining cell area.⁴⁶

To study cell migration, HSCs at 75% confluency were trypsinised and plated into 24 well plates at a density of 5,000 cells per well with 16% growth medium and incubated overnight at 37°C. The next day, plates were loaded onto a wide field microscope with time-lapse capability (Nikon LT TL). NIS-Elements AR software (Nikon) was used to acquire images from predetermined points at \times 20

magnification every 10 min over a 24-h period. Image sequences were analyzed using ImageJ software. The MTrackJ plug-in (ImageJ) was used to track cell movement over the 24-h period. To determine relative cell migration, six random cells were tracked, and the total cell track distance was measured. For individual cells, the co-ordinates at each 10-min interval were made relative to a starting point (0,0) and plotted to give representative distance graphs. Measurements in ImageJ were generated in arbitrary units.^{3,46} Directionality was determined by calculating the hypotenuse length of the triangle outlined by the minimum and maximum positions on the x and y axis.

For gel contraction assays, HSCs in culture were detached using trypsin, centrifuged and resuspended in 16% growth medium at a density of 40,000 cells per mL. In a 12-well plate collagen gels were created using 295 μ L of rat tail collagen (Corning), 6.66 μ L of newly titrated 1M NaOH and 700 μ L of HSCs in 16% growth medium per gel. Plates containing the seeded gels were incubated at 37°C for 1 h. After solidifying, gels were transferred into a well of a 6-well plate containing 3mL of prewarmed media while avoiding tearing or folding in the gel. Images were taken at 0 h and 24-h, following incubation at 37°C, using the colorimetric imaging settings of a trans-illuminator (Bio-Rad). To measure contraction, ImageJ software (ImageJ) was used to draw a circle around the internal edge of the well and the perimeter of the gel at each time point. Gel sizes were calculated as a percentage of the well area, and contraction calculated as the percentage change between 0 h and 24 h.

Atomic force microscopy (AFM)

AFM experiments were performed on a Nanowizard IV AFM (JPK) mounted on an Axio Observer.A1 (Zeiss) inverted optical microscope, with a Vortis Controller (JPK) using SPM Desktop software v6.1.65 (JPK). Isolated WT and *Pak1*-null HSCs were plated onto fibronectin-coated glass dishes for live cell imaging, or fibronectin coated glass coverslips for fixed cell analysis. For live cell analysis, samples were held in a heated Petri dish holder during measurements. For fixed cell analysis, cells were fixed in 2.5% glutaraldehyde at the indicated time point and stored under PBS until analysis. Mechanical data was obtained in fluid using 5 μ m diameter gold colloidal probes (CP-CONT-AU-B, sQUBE, Germany) mounted on cantilevers with a nominal spring constant of 0.3N/m; exact values for cantilever spring constants were determined prior to data acquisition using the JPK non-contact method. Force curves were analyzed using JPK Data Analysis software to calculate the average Young's Modulus of the nucleus based on the Hertz model. When comparing between groups (e.g., *Pak1*-null vs. WT), measurements were taken with a consistent setpoint and approach velocity for all nuclei analyzed and using the exact same probe.

RNA microarray

HSCs were isolated from WT and *Pak1*-null mice and RNA was extracted on day 0 (quiescent) or after 10 days (activated) of culturing on plastic. RNA was extracted as previously described and stored at -80° . The integrity of RNA samples was assessed, and samples were considered of sufficient quality when having an RNA integrity number (RINe) of ≥ 6.5 . An Affymetrix mouse genome 430 2.0 array using 2894 probe sets was employed for this experiment. Data was initially assessed using principal component analysis (PCA) to determine the source of variation in results, before undergoing cluster analysis. Subsequent datasets were then examined using online bioinformatic analytical software. The Database for Annotation, Visualization and Integrated Discovery (DAVID) analysis version 6.8 (<https://david.ncicrf.gov/>) was used for functional annotation and gene ontology analysis, whilst Ingenuity Pathway Analysis (<https://www.qiagenbioinformatics.com>) was employed to identify key canonical pathways between experimental groups.

Cut&Tag

Cut&Tag was performed using a Complete CUT&Tag-IT Assay Kit (Active Motif) according to manufacturer's instructions. For each reaction of quiescent samples, 500,000 cells were counted from a pool of freshly isolated HSCs from three mice. For activated samples, mouse HSCs were cultured on plastic for 7 days and collected by brief incubation at 37° in 0.05M EDTA in HBSS to promote detachment followed by cell scraping. For each activated reaction, 500,000 cells were counted from a pool of HSCs from three mice. Briefly, cells were attached to concanavalin A beads before overnight binding of primary antibody. 'H3K9Me3 antibody 1' refers to 39765 (Active Motif), 'H3K9Me3 antibody 2' refers to 13969 (CST) and the H3K27Me3 to 39155 (Active Motif). This preceded binding of secondary antibody and CUT&Tag-ITAssembled pA-Tn5 Transposomes, tagmentation and purification of tagmented DNA. This DNA was PCR amplified using a unique combination of i5/i7 indexing primers for each sample, cleaned using SPRI beads and pooled into an equimolar library for sequencing on an Illumina HiSeq4000 sequencing platform.

Unmapped paired-end reads of 76bp were checked using a quality control pipeline consisting of FastQC v0.11.3 (<http://www.bioinformatics.babraham.ac.uk/projects/fastqc/>) and FastQ Screen v0.14.0 (https://www.bioinformatics.babraham.ac.uk/projects/fastq_screen/). Reads were trimmed to remove any remaining adapters and poor quality sequence using Trimmomatic v0.39⁴⁷; reads were truncated at a sliding 4bp window, starting 5', with a mean quality <Q20, and removed if the final length was less than 35bp. Additional flags included: 'ILLUMINACLIP:./Truseq3-PE-2_Nextera-PE.fa:2:30:10 SLIDINGWINDOW:4:20 MINLEN:35'.

Paired-reads were mapped to the mouse genome (mm39/GRCm39)⁴⁸ using Bowtie2 v2.4.2.⁴⁹ samtools v1.12⁵⁰ was used to create (view) and sort (sort) BAM files from the SAM files output from Bowtie2. Reads located in blacklist regions were removed using bedtools intersect v2.27.1.⁵¹ Blacklist regions for mouse mm10 (<https://github.com/Boyle-Lab/Blacklist/blob/master/lists/mm10-blacklist.v2.bed.gz>) were converted to mm39 using UCSC liftOver, the 'Minimum ratio of bases that must remap' was set to 0.95. The reads were then filtered to retain only concordant read pairs with a minimum quality score of 2, using samtools view (-f2 -q2).

Prior to peak calling read pairs were removed that mapped to the mitochondrial genome or unassembled contigs, using the Linux bash tool 'sed' (sed '/chrM/d; /random/d; /chrUn/d; /GL456/d; /JH584/d; /MU069/d'). Candidate binding regions 'peaks' were identified using SEACR v1.3.⁵² The software was run in both 'relaxed' and 'stringent' modes. In both sets of fragment counts were normalised 'norm', and the top 1% of regions were selected. The closest gene was associated with each region using RnaChIPIntegrator v2.0.0 (<https://github.com/fls-bioinformatics-core/RnaChIPIntegrator>) (-cutoff = 100000 -edge = both -number = 1 -compact). The gene annotation for Gencode vM27/mm39 (knownCanonical) was downloaded using the UCSC table browser.

ATAC-seq/RNA-seq

Accessible genomic DNA was obtained for sequencing using an ATAC-seq kit (Active Motif) as per manufacturer's instructions. 100,000 freshly isolated mHSCs were used for each quiescent reaction. For activated samples, mHSCs were cultured on plastic for 7 days and collected by brief incubation at 37° in 0.05M EDTA in HBSS to promote detachment followed by cell scraping, and 100,000 cells used for each reaction. Cells were pelleted, washed with PBS then resuspended in ATAC lysis buffer. Nuclei were pelleted by centrifugation at 500 g at 4° before resuspension in tagmentation buffer and incubation at 37° for 30 min. DNA was then purified and each sample amplified with a unique combination of i5/i7 primers for 10 cycles followed by SPRI clean-up and pooling into an equimolar library. In parallel, RNA was extracted from quiescent and activated cells using an RNeasy kit (Qiagen) for RNA-seq.

For ATAC-seq, unmapped paired-reads of 76bp from an Illumina HiSeq4000 sequencer were QC checked as described for Cut&Tag and removed if the final length was less than 25bp. Paired-reads were mapped to the mouse genome as described for Cut&Tag, using additional parameters ('-X 2000 -very-sensitive'). Picard v2.1.0 MarkDuplicates (<https://broadinstitute.github.io/picard/>) was used to remove duplicate reads on the same strand. Mitochondrial reads and reads located in blacklist regions were removed as described for Cut&Tag. ATAC-seq fragment length quality plots were generated using ATACseqQC v1.12.5⁵³ in R v4.0.2 (R Core Team 2021). Candidate regions of open chromatin 'peaks' were identified using MACS2 v2.2.7.1⁵⁴ using additional parameters (-format BAMPE -gsize mm -keep-dup all -qvalue 0.01 -bdg -SPMR -call-summits). DNA fragment coverage profiles generated by MACS2 were converted into bigWig and bigBed format using the UCSC tools bedClip, bedGraphToBigWig, and bedToBigBed.

Differential binding analysis was performed using DiffBind v3.4.11⁵⁵ in R v4.1.2. The 'peak' input consisted of 200bp regions centered on MACS2 summit coordinates, in BED format, together with the qvalue of each region (chr, start, end, q-value). The 'read' input were the final filtered BAM files used in the MACS2 peak calling. dba.count parameters were set differently from the default (minOverlap = 2, summits = FALSE).

UCSC knownCanonical genes from Gencode Mouse v27 were associated with Diffbind regions using RnaChIPIntegrator v2.0.0, including the following parameters (-cutoff = 100000 -edge = both -number = 2 -compact). In order to identify DiffBind regions in the promoters of genes the following parameters were used (-cutoff = 100000 -edge = tss -number = 1 -compact).

For RNA-seq, unmapped paired-reads of 51bp from a NovaSeq6000 were QC checked and trimmed as previously and removed if the final length was less than 35bp. Additional flags included: 'ILLUMINACLIP:./Truseq3-PE-2_Nextera-PE.fa:2:30:10'. The filtered reads were mapped to the mouse reference sequence analysis set (mm39/GRCm39) from the UCSC browser (Kent et al. 2002), using STAR v2.7.7a (Dobin et al. 2013). The genome index was created using the comprehensive mouse Gencode v27 gene annotation (Harrow et al. 2012) applying a read overhang (-sjdbOverhang 75). During mapping the flags '-quantMode GeneCounts' was used to generate read counts into genes. Normalisation and differential expression analysis was performed using DESeq2 v1.34.0 on R v4.1.2 (Love, Huber, and Anders 2014). A single factor was included in the model to compare activated versus quiescent cells. Log fold change shrinkage was applied using the lfcShrink function along with the "apeglm" algorithm.

EnrichR was used to identify significantly enriched GO terms within filtered gene lists.⁵⁶ Simple Enrichment Analysis from the MEME suite toolset was used to identify enriched TF motifs within promotor ATAC peaks.⁵⁷

QUANTIFICATION AND STATISTICAL ANALYSIS

Statistical analyses were performed using GraphPad Prism 9 software using the indicated tests. Shapiro-Wilks tests were used to assess normality of data. Where data were normally distributed, two-tailed student t-tests were used for pairwise analyses and one-way ANOVA with Tukey's post hoc test for comparisons across more than two groups. For non-normally distributed data, Mann-Whitney testing was used for pairwise analysis. Correlation analysis was assessed using a 2-parameter exponential regression model (R-squared).